The Finescale Response of Lowered ADCP Velocity Profiles

KURT POLZIN

Woods Hole Oceanographic Institution, Woods Hole, Massachusetts

ERIC KUNZE

School of Oceanography, University of Washington, Seattle, Washington

JULES HUMMON AND ERIC FIRING

JIMAR, University of Hawaii, Honolulu, Hawaii

(Manuscript received 13 March 2000, in final form 20 April 2001)

ABSTRACT

Lowered acoustic Doppler current profiler (LADCP) velocity profiles are compared with simultaneous higher-resolution expendable current profiler (XCP) profiles to determine the lowered ADCP's response at short wavelengths. Although lowered ADCP spectra are attenuated in comparison to XCP spectra for vertical wavelengths as large as 150 m, the signals are coherent for wavelengths between 50 and 1200 m. A model spectral transfer function based on the expected response for the lowered ADCP reproduces the observed attenuation. Spectrally corrected LADCP data can be used to infer turbulent eddy diffusivities to within a factor of 3–4 using a finescale parameterization.

1. Introduction

In recent years, a number of investigators have attached acoustic Doppler current profilers (ADCPs) to rosette frames to obtain full-water-depth velocity profiles in conjunction with hydrographic casts (Schott et al. 1993; Fischer and Visbeck 1993; Hinrichsen et al. 1994; Send 1994; Wilson et al. 1994; Fischer et al. 1996; Hacker et al. 1996; Stramma et al. 1996; Beal and Bryden 1997; Hufford et al. 1997; Firing et al. 1998). Coverage to date includes $O(3000)$ profiles along many hydrographic sections in the Indian, South Pacific, and North Atlantic Oceans (Chapman 1998). As well as providing profiles of large-scale flow, these sample the oceanic internal-wave field at vertical wavelengths $\lambda_z > 50$ m.

Our motivation for this study is to define the finescale ($10\text{s} < \lambda_z < 100\text{s}$ m) information content of these lowered ADCP profiles. The finescale internal wave spectral level has been used to infer turbulent kinetic energy dissipation rates ε and eddy diffusivities K (Gregg 1989; Polzin et al. 1995; Sun and Kunze 1999). These finescale parameterizations for turbulence may permit quantification of abyssal mixing over a wide variety of topography undersampled by microstructure measurements. Determining mixing in the World Ocean is an important step toward closing the thermohaline circulation and modeling large-scale ocean dynamics correctly (Marotzke 1997; Samelson 1998; Munk and Wunsch 1998).

Recent work (Gregg 1989; Ledwell et al. 1993; Toole et al. 1994; Kunze and Sanford 1996; Polzin et al. 1997) has established that mixing in the stratified ocean interior over abyssal plains is an order of magnitude smaller than basin-scale bulk estimates (Hogg et al. 1982) or those inferred from a global vertical advective–diffusive balance (Munk 1966; Munk and Wunsch 1998). It has been suggested that, rather than being uniformly distributed, ocean mixing might be concentrated over rough or steeply sloping topography. Elevated turbulent mixing is observed above seamounts (Kunze and Toole 1997; Lueck and Mudge 1997; Eriksen 1998), ridges (Polzin et al. 1997; Althaus et al. 1999), and in constrictive passages (Polzin et al. 1996; Roemmich et al. 1996). Interactions of mesoscale eddy, barotropic tidal, and internal-wave currents with topographic roughness are expected to augment the abyssal internal-wave and turbulence fields. But this parameter space remains undersampled. A census of turbulence over the wide variety of topographic and flow regimes contained in extant lowered ADCP datasets would go a long way toward establishing basin-average abyssal mixing levels.

Existing lowered ADCP profiles provide wider coverage of abyssal waters than is available from direct microstructure measurements. While they would pro-

Corresponding author address: Dr. Kurt Polzin, Woods Hole Oceanographic Institution, Woods Hole, MA 02543.
E-mail: kpolzin@whoi.edu

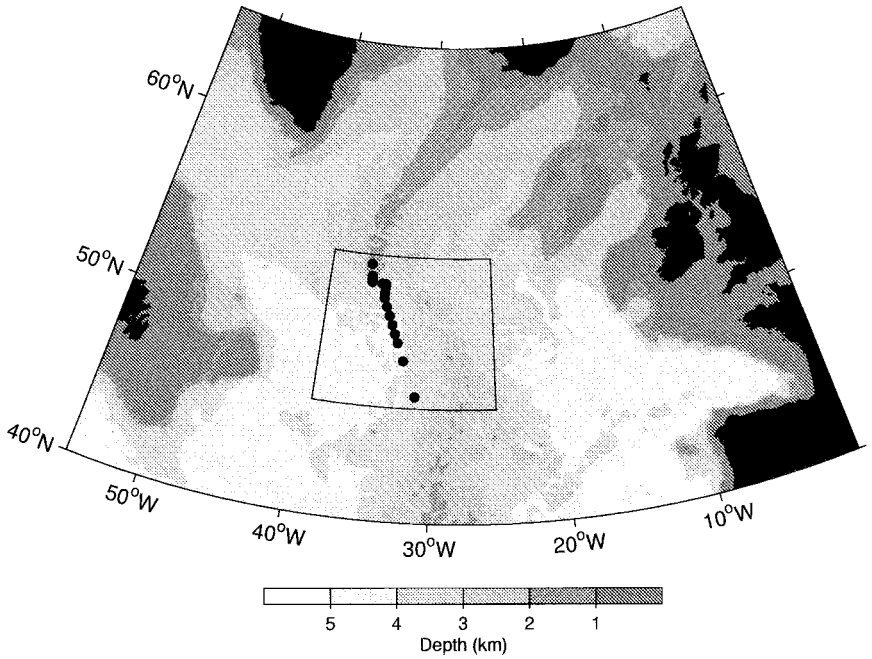

FIG. 1. Locations of lowered ADCP–XCP pairs along the western flank of the Mid-Atlantic Ridge in the vicinity of the Gibbs Fracture Zone. Numbers correspond to stations of the hydrographic section.

vide less accurate estimates of the turbulent dissipation rate, the broad coverage presently available argues for analysis of these data. Such analysis may also help design future micro- and fine structure field studies. A pilot study using lowered ADCP data from east of the Kerguelen Plateau (Polzin and Firing 1997) demonstrated the feasibility of this approach, finding middepth turbulent diffusivities of 0.2×10^{-4} m^2 s^{-1} at 35°S and 4.4×10^{-4} m^2 s^{-1} at 55°S.

The finescale response of ADCPs is not well known, however. In this paper, lowered ADCP profiles will be compared with a velocity profiler of better-known performance, the Sippican expendable current profiler (XCP) (Sanford et al. 1982, 1993). A model spectral transfer function that takes into account spatial averaging inherent in lowered ADCP measurement and data processing reproduces the observed finescale attenuation of the lowered ADCP spectrum inferred from comparison with the XCP spectrum.

2. Data

Eighteen lowered ADCP–XCP profile pairs were collected during November 1997 on a hydrographic section spanning 46°37′–53°30′N, 31°13′–35°30′W. The majority of these profiles were obtained above the Mid-Atlantic Ridge in the vicinity of the Gibbs Fracture Zone (Fig. 1). Stratification was weak, with buoyancy frequencies $N = (1–3) \times 10^{-3}$ rad s^{-1} below 200-m depth.

The XCP measures horizontal velocities relative to an unknown but depth-independent constant by measuring the voltage drop across its insulating body induced by the motion of conducting seawater through the Earth's magnetic field (Sanford et al. 1982, 1993). It profiles from the surface to 1600-m depth. Depth is inferred from the time since deployment using a quadratic fall speed formula with nominal relative depth uncertainties of 10%. Based on raw 0.3-m resolution profiles, the vertical wavenumber spectrum for velocity noise in XCP profiles is white with a level 0.72×10^{-4} m^2 s^{-2} (rad m^{-1})$^{-1}$ (Sanford et al. 1982; see dotted diagonal line in Fig. 5), corresponding to rms uncertainties of 1.5 (0.7) cm s^{-1} integrated to a Nyquist wavelength of 2 (10) m. This random noise in velocity arises from instrument vibration, electronic and electrode noise. In these data, the signal hits the noise floor at $\lambda_z = 30$ m; this is longer than the 10 m found for midlatitude measurements (Sanford et al. 1982) because of weaker stratification. In addition, the XCP rotation rate exhibits fluctuations at vertical wavelength $\lambda_z = 20–30$ m associated with fall rate fluctuations, which may affect the meridional velocity (Sanford et al. 1993).

The XCPs were deployed so as to pass as close as possible to the CTD package as both instruments crossed 1000-m depth. While the lowered ADCP gathers data during both up- and downcasts, XCPs were deployed only during downcasts. For many profile pairs, they passed close enough that the XCP's sensitivity to the electric field of the CTD package precludes using its measurements within ±100 m of the depth where the two instruments crossed. This part of the XCP profile

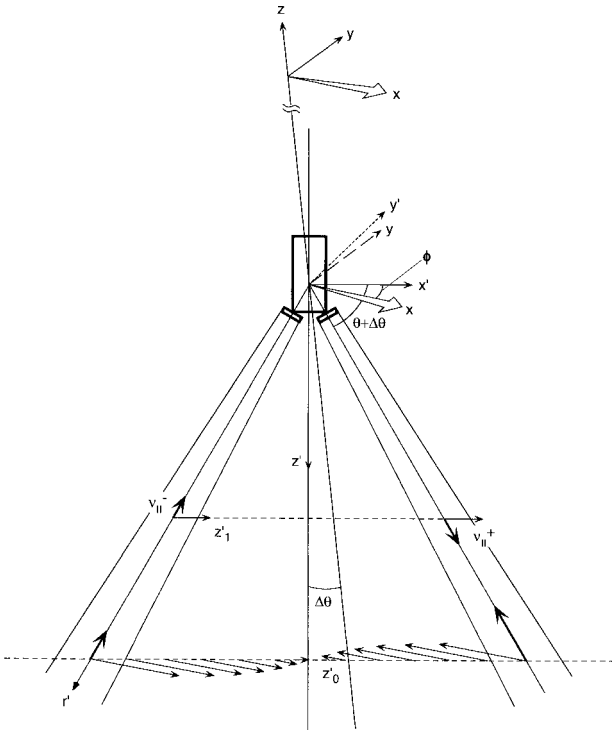

FIG. 2. Schematic of the lowered ADCP measurement geometry. The x, y, z coordinates are geographic, centered on the lowered ADCP station with depth z positive *upward* and zero at the ocean surface. The x', y', z' coordinates are centered on the lowered ADCP platform with vertical range $z' = r' \sin\theta$ positive *downward,* and the horizontal axes x' and y' rotated by ϕ about the vertical axis. In the x', z' plane, where x' and z' represent horizontal and vertical ranges from the instrument, two acoustic beams are slanted at a downlook angle of $\theta = 60°$ from the horizontal, measuring slant velocities $v_\parallel^+$ and $v_\parallel^-$ (thick alongbeam arrows). Thin arrows at vertical range $z' = z'_1$ depict horizontally uniform flow while thin arrows at z'_0 depict horizontal and vertical velocities of an internal wave with horizontal wavelength twice the beam separation. The ADCP estimate of horizontal velocity will be in error if the oceanic velocity field is horizontally nonuniform as depicted at z'_0. The models for the instrument response (section 4) assume the lowered ADCP package is located at (x, y, z) = (0, 0, z_{ADCP}). The tilt model [section 4a(d)] assumes rotation ϕ about the z' axis and a tilt $\Delta\theta$ about the y' axis.

was replaced by a linear interpolation in subsequent analysis.

The ADCP does not measure horizontal velocity at a point but determines Doppler shifts as a function of range along four acoustic beams typically slanted at an angle $\theta = \pi/3 = 60°$ from the horizontal plane (Fig. 2) and spaced at 90° intervals around the compass (Janus configuration). These Doppler shifts are interpreted as slant velocities of suspended acoustic backscattering targets moving with the water relative to the instrument platform. Each pair of opposing slant velocities, $v_\parallel^+$ and $v_\parallel^-$, is combined to produce estimates of vertical velocity

$$w_{\text{ADCP}} = \frac{v_\parallel^+ + v_\parallel^-}{2 \sin\theta} \tag{1}$$

and horizontal velocity

$$u_{\text{ADCP}} \quad \text{or} \quad v_{\text{ADCP}} = -\frac{v_\parallel^+ + v_\parallel^-}{2 \cos\theta} \tag{2}$$

under the assumption that the flow field is horizontally uniform over the beam separation. Likewise,

$$v_\parallel^+ = -u(x^+) \cos\theta + w(x^+) \sin\theta;$$

$$v_\parallel^- = u(x^-) \cos\theta + w(x^-) \sin\theta.$$

The difference between the independent estimates of vertical velocity from the two orthogonal beam pairs is referred to as the error velocity and provides a consistency check. As a function of vertical range below the instrument z', the beams are separated in the horizontal by a distance $2x' = 2z' \cot\theta$; for a typical vertical range $z' = 160$ m, the beam separation $2x' = 185$ m. Horizontal uniformity of the flow on this scale is not an unreasonable assumption since the dominant horizontal currents in the ocean are near-inertial internal waves, internal tides, and geostrophic flows, all of which typically have aspect ratios $k_h/k_z = \lambda_z/\lambda_h = f/N$ or lower (where $f = 1.1 \times 10^{-4}$ rad s^{-1} is the Coriolis frequency and $N = 1.7 \times 10^{-3}$ rad s^{-1} the buoyancy frequency) so that $\lambda_h \gg 200$ m for $\lambda_z > 200$ m ($\lambda_h = 750$ m for $\lambda_z = 50$ m). However, high-frequency and high-vertical-wavenumber internal waves have shorter horizontal scales, particularly at low stratification. If the flow field is horizontally nonuniform, that is, $u^+ \neq u^-$ and $w^+ \neq w^-$, the horizontal velocity estimate will be contaminated by horizontal variability in both the horizontal velocity $u(x)$ and the vertical velocity $w(x)$. The present study shows that such horizontal variability does not impair the utility of lowered ADCP profiles at vertical wavelengths $\lambda_z > 50$ m.

The ADCP used for this study was a broadband, or coherent, 150-kHz sonar made by RD Instruments that uses coded pulses (Pinkel and Smith 1992). The beam configuration was optimized for range rather than vertical resolution. Bandwidth was set to 9% (WB1 command in RDI 1996 parlance) and the simplest profiling mode (WM1 in RDI parlance) was used with the maximum fixed ambiguity interval at about 3.3 m s^{-1}. The transmitted pulse Δz_t and receiver processing bin lengths Δz_r are both 16 m in the vertical, as was the blanking interval after transmission. Intervals between pings alternate between 1.0 and 1.6 s so that interference from the return of previous pings from the ocean bottom occurs at different depths on alternate pings. Bottom interference can then be edited out without leaving a gap in the profile. The single-ping accuracy for each horizontal velocity component is estimated to be 3.2 cm s^{-1} based on the observed variance in velocity component first-differences and the error velocity. Repeated sampling and bin averaging, typically over 120 pings in this data, are necessary to reduce this uncertainty. Smoothing over currents of small vertical and horizontal scales is intrinsic to the lowered ADCP's sampling because of the instrument's finite resolution and its motion.

Single-ping profiles are ~250 m long. Absolute full-depth velocity profiles were assembled from overlapping single-ping profiles as described by Fischer and Visbeck (1993) but with some differences in implementation (section 4a). The unknown motion of the instrument platform was removed by first-differencing in the vertical to obtain profiles of vertical shear. First-differencing removes translational motions of the instrument but not the effect of instrument tilts. Shears were then interpolated onto a uniform 5-m grid and averaged over all pings in given depth intervals. The composite full-depth shear profile was integrated to yield a velocity profile with the constant of integration determined from the time integral of flow past the package and the net displacement of the package over the ground during the cast. Instrument depth was obtained from CTD pressure. Alignment of CTD and ADCP profiles was achieved by matching vertical velocity from the ADCP to the time derivative of pressure from the CTD; this was originally done because poor CTD clocks prevented matching ADCP and CTD profiles and this procedure is still part of the automated processing. Alignment accuracy of 1 s or better is possible because of the large signal in w due to ship heave in ocean swell. However, after aligning CTD and XCP temperature profiles, comparison between lowered ADCP and XCP velocity profiles suggests additional rms profile-to-profile depth offsets of 8 m. Since XCP drops were not precisely simultaneous with lowered ADCP profiles in time and space, some of this difference may be associated with horizontal variability, some with internal-wave vertical motions contributing to the ADCP vertical velocity estimates.

The present method of interpolating the shear onto a 5-m grid affects the vertical wavenumber transfer function [section 4a(3)], so requires a detailed description. After converting from range to depth coordinates, each shear calculated from the difference between velocities in adjacent depth bins is assigned to the midpoint between the depth bins. Individual shear profiles are then taken as piecewise-linear continuous functions of depth by interpolating between these point shear estimates. Finally, individual shear profiles are box-averaged in 5-m intervals centered on the standard 5-m grid points of the composite profile. Typically, this corresponds to a ~100-s average while the instrument descends past the depth bin.

Only downcasts are used in this study of instrument response. After rejecting shear and velocity outliers, composite downcast shear profiles were typically based upon 120 or more shear estimates at each depth. The number of shear estimates is a function of the effective range of the lowered ADCP, which depends on the number of scatterers. Extensive experience on other World Ocean Circulation Experiment (WOCE) cruises has shown that scattering varies widely from region to region. Lack of scatters below 1000 m in subtropical gyre interiors and parts of the Tropics reduces lowered ADCP ranges to the point that profiling is difficult or impossible. Scattering is better in western boundary currents and better yet in subpolar gyres such as the data described here. In the upper 2000 m, there were often valid velocity estimates in all 16 range bins.

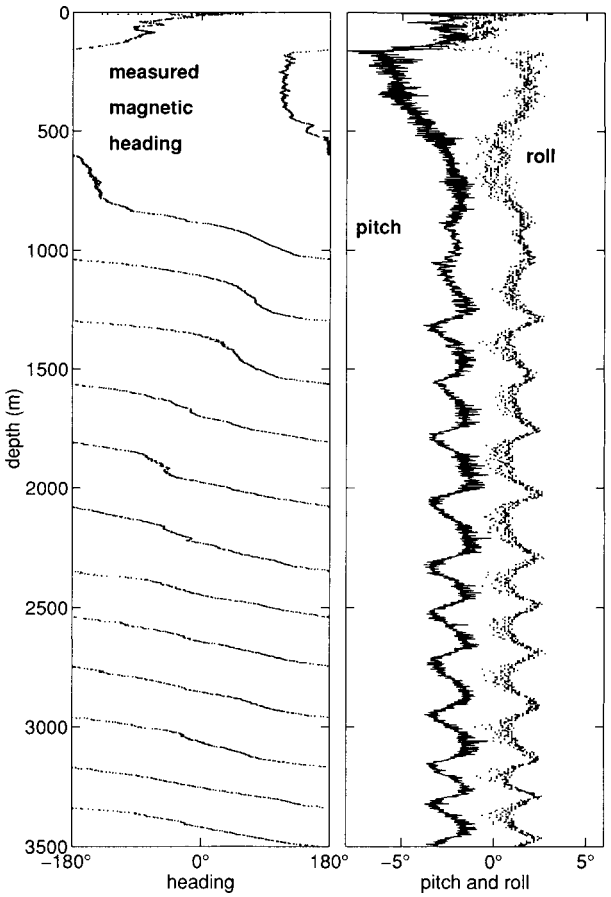

FIG. 3. Typical depth profile of measured magnetic heading, pitch, and roll. The instrument descent rate is approximately 1 m s^{-1}. Pitch and roll represent tilting of the instrument in planes defined by the acoustic beams. Pitch and roll exhibit an $O(1°)$ high-frequency jitter superimposed on a lower-frequency oscillation that is coherent with compass heading.

A final issue affecting instrument performance is package motion. Rotation, tilting, and lowering of the instrument cause the acoustic beams to sweep out areas in the horizontal plane, smoothing the data. The Rosette frame to which the ADCP package is attached tends to rotate as it is lowered due to unwinding of the cable and torques exerted by flow past the asymmetric package. In this dataset, rotation varies from 0 to $2\pi/50$ rad m^{-1} and defies succinct description (Fig. 3). Pitch and roll represent tilting of the instrument in the planes defined by opposing acoustic beams. The measured tilt arises from (i) the static balance of the instrument package when suspended in the water, (ii) instrument orientation relative to the Rosette frame, (iii) hydrodynamic forces induced by flow past the package, and (iv) the (mainly vertical) motion of the wire due to lowering

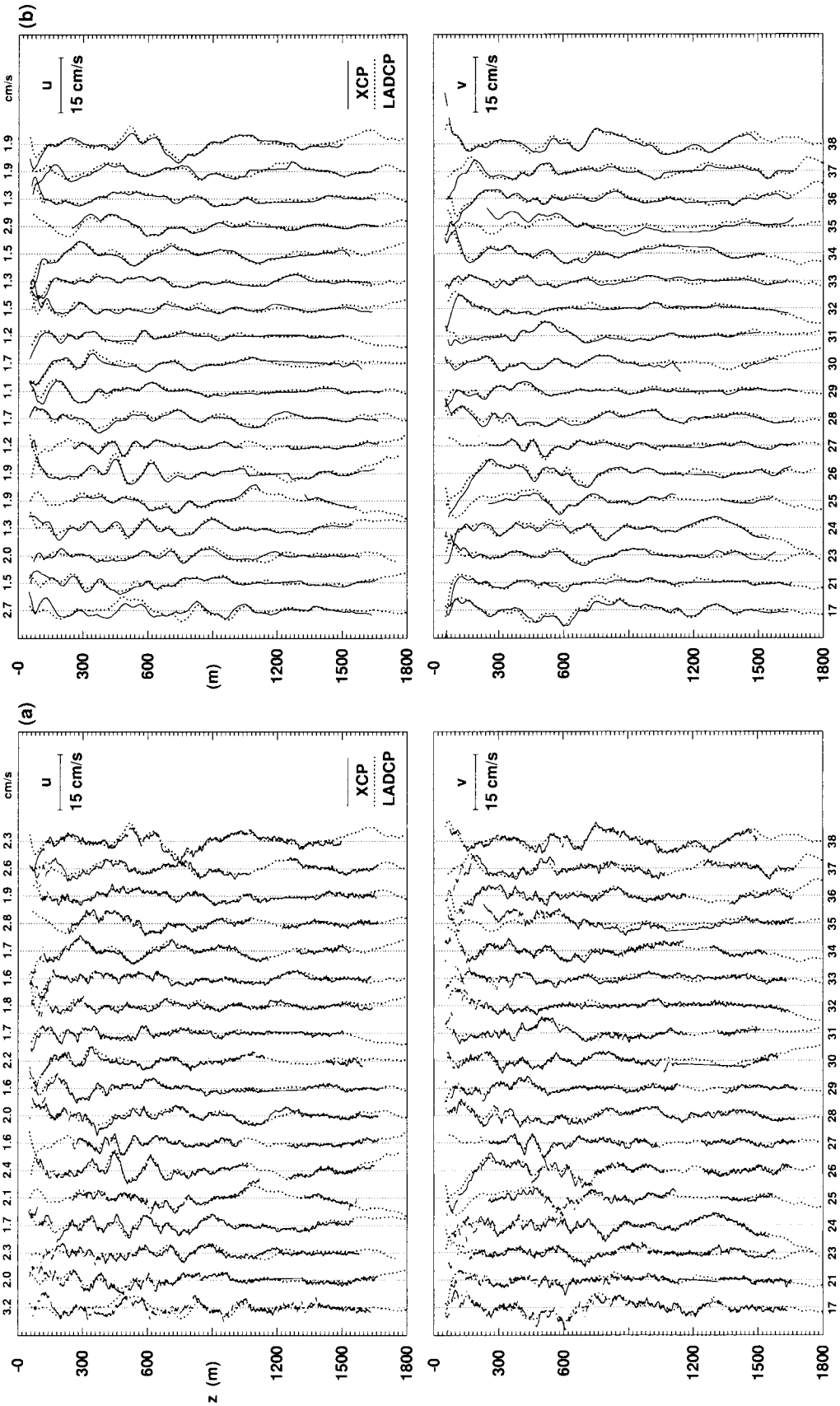

FIG. 4. Comparison between simultaneous XCP (solid) and LADCP (dotted) u (top) and v (bottom) velocity profile pairs. Numbers along the upper axis are rms velocity differences between the two profiles. (a) The 2-m binned XCP and 5-m binned lowered ADCP profiles. Quadratic fit profiles have been removed from all profiles, and the depth coordinate for the XCP profiles has been linearly stretched and offset to minimize the rms velocity difference between the profile pairs. Gaps between 1100- and 1300-m depth in some of the XCP profiles are data contaminated by the electric field of the CTD–LADCP package. (b) XCP data smoothed with a 20-m running boxcar.

and wave-induced ship heave. The magnitude of the tilt $(=\text{pitch}^2 + \text{roll}^2)^{1/2}$ exhibits a slowly varying component of 3°–4° and high-frequency jitter of less than 1°.

3. Comparison of velocity profiles

XCP and lowered ADCP (LADCP) velocity profile pairs are displayed in Fig. 4. Prior to plotting in Fig. 4a, a quadratic fit was removed from both velocity profiles and the XCP profiles vertically offset and stretched linearly so as to minimize the rms velocity difference between XCP and lowered ADCP profiles. This is necessary as the XCP fall rate is a function of time that is not precisely known, and the XCP and lowered ADCP profiles are not precisely simultaneous in time and space. A more sophisticated depth-offsetting procedure, such as the high-vertical-wavenumber lagged correlation approach of Prater (1991), was deemed unnecessary. When additionally the XCP profile is smoothed with an ad hoc 20-m boxcar, the profile pairs closely resemble each other (Fig. 4b).

Further analysis is carried out in spectral space. The 2-m resolution XCP profiles were interpolated and resampled at 2.5-m intervals to match lowered ADCP sample depths. Then the 5-m lowered ADCP and 2.5-m XCP profiles were Fourier transformed over 220–1500 m (256 and 512 points, respectively).

Average vertical wavenumber spectra for buoyancy frequency-normalized shear $V_z/\overline{N}$ (where $V_z = \sqrt{u_z^2 + v_z^2}$) are compared in Fig. 5 where the average buoyancy frequency $\overline{N} = 1.7 \times 10^{-3}$ rad s^{-1} in this depth range. Counterclockwise-with-depth variance dominates over clockwise by a factor of 1.2–1.3 (not shown), implying more up- than downgoing near-inertial energy. This may be related to generation or scattering of internal waves from underlying topography. XCP and lowered ADCP spectra closely resemble each other for wavelengths $\lambda_z > 150$ m. The lowered ADCP spectrum becomes increasingly attenuated relative to the XCP spectrum at smaller wavelengths, and is an order of magnitude below the XCP spectrum by $\lambda_z = 50$ m.

However, coherence between XCP and lowered ADCP signals remains high and is significantly different from zero (Fig. 6a) with phase differences near zero (Fig. 6b) for all vertical wavelengths $\lambda_z > 50$ m. This suggests that the attenuated LADCP signal for wavelengths $\lambda_z > 50$ m (Fig. 5) can be spectrally corrected. At smaller wavelengths, the coherence drops to insignificance.

The spectral transfer function between LADCP and XCP signals $T(k_z)$ is taken to be just the ratio of the spectra in Fig. 5. For wavelengths $\lambda_z > 150$ m, the spectral transfer function is about 1.0. At shorter wavelengths, the inverse of the transfer function $T(k_z)$ rises steeply. A least squares fit to the data gives the empirical spectral transfer function

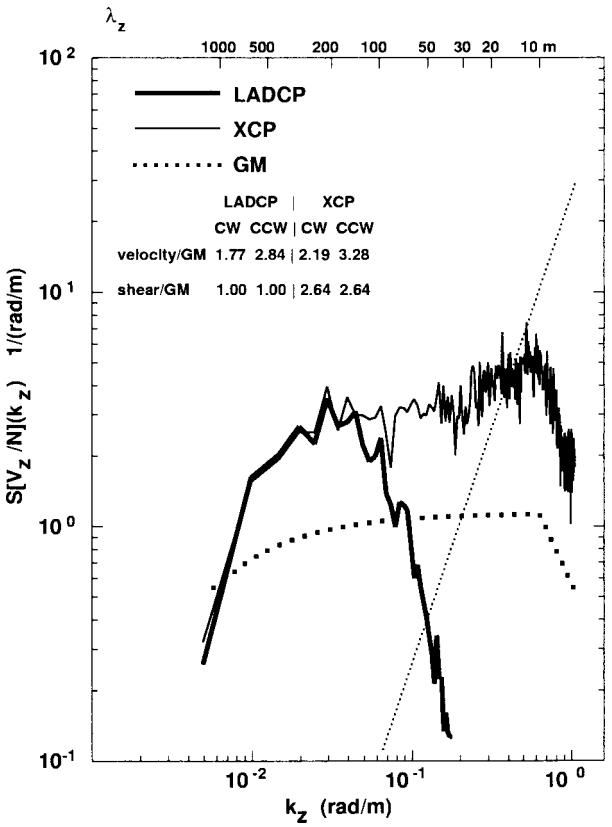

FIG. 5. Vertical wavenumber spectra for buoyancy-frequency-normalized shear V_z/N from the depth range 220–1500 m. Vertical wavelengths are marked along the upper axis. Measured spectra have been smoothed with overlapping $0.1 - \log(k_z)$ intervals. The smooth thick dotted curve is the GM model spectrum with peak mode number $j^* = 3$, the thick solid curve from 18 lowered ADCP profiles, and the thin solid curve from the simultaneous XCP profiles. The XCP spectrum is contaminated by instrument noise to the right of the thin dotted diagonal, i.e., for vertical wavenumbers $k_z > 0.3$ rad m^{-1} ($\lambda_z < 20$ m) raw XCP instrumental noise, which is blue as k_z^2 in shear, has been reduced at high wavenumbers in the processed profiles used for this spectrum. Numbers in the upper left quadrant indicate GM-normalized clockwise- and counterclockwise-with-depth velocity variance from the lowered ADCP and XCP spectra (upper row), and clockwise and counterclockwise shear (lower row) for wavenumbers $k_z < 0.2$ rad m^{-1} ($\lambda_z > 30$ m). XCP spectral levels are roughly three times GM. LADCP levels become increasingly attenuated for wavenumbers $k_z > 0.04$ rad m^{-1} ($\lambda_z < 150$ m) and is down by a factor of 10 at $\lambda_z = 50$ m.

$$T(k_z) = \frac{S_{\text{LADCP}}(V_z/N)(k_z)}{S_{\text{XCP}}(V_z/N)(k_z)} = 10^{-50 \cdot k_z^2} \qquad (3)$$

(Fig. 7). This curve agrees to within 10% with a model curve (dashed) described in the next section (30) that takes into account vertical smoothing due to range averaging over transmit and receive intervals, first-differencing to remove package motion, interpolation, and bin mapping associated with instrument tilt. Horizontal smoothing associated with beam-separation effects has less impact.

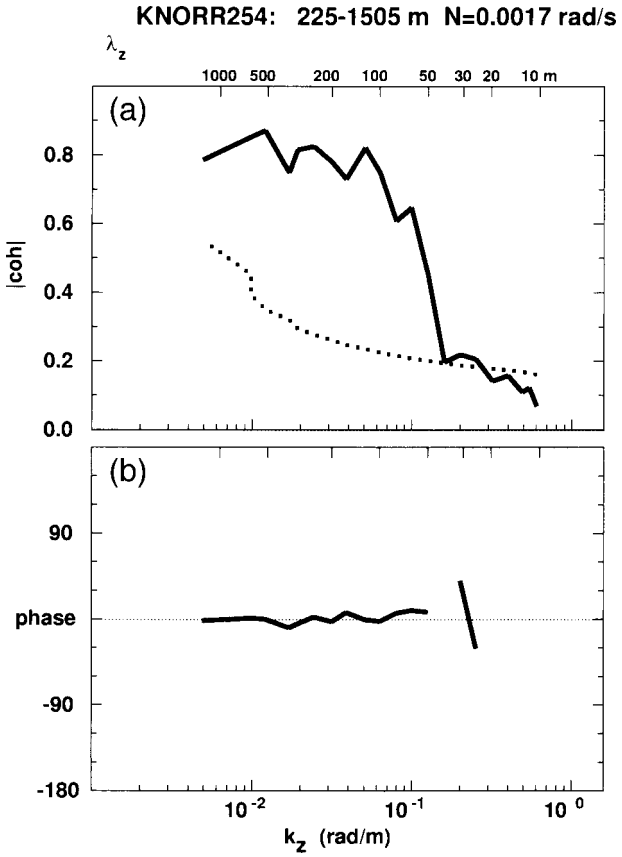

FIG. 6. (a) Coherence magnitude |coh| and (b) phase between the 18 simultaneous XCP and lowered ADCP velocity profiles. The coherence is significantly different from zero for $\lambda_z > 50$ m; the dotted curve is the 95% confidence. Phase is not significantly different from zero where the coherence is significant.

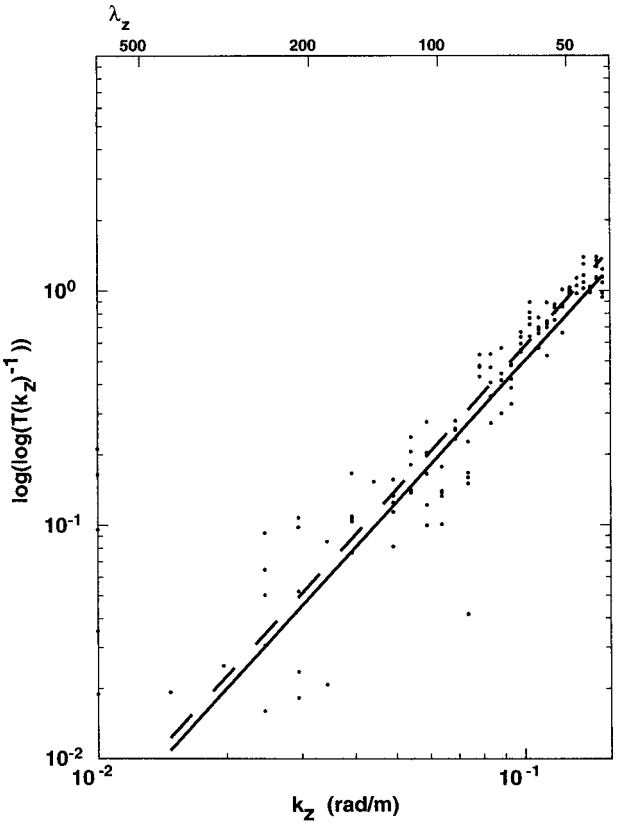

FIG. 7. Observed spectral transfer function inverse $T(k_z)^{-1}$ [(3)] for LADCP measurements relative to XCP measurements (dots). LADCP and XCP estimates are identical for low vertical wavenumbers $k_z < 0.02$ rad m^{-1} ($\lambda_z > 300$ m) and rise sharply at higher wavenumbers. A least squares fit [(3)] (solid line) to the observed transfer function (dots) lies within 10% of a modeled response, which neglects beam-separation effects [(30)] (dashed line).

4. Modeling the lowered ADCP response

The lowered ADCP response is a function of the sensor geometry, sampling strategy, data processing, and package motion. This section attempts to quantitatively model the resulting attenuation of oceanic shear.

The ADCP estimates alongbeam velocities from Doppler shifts as a function of range along four slanted beams. These along–beam velocities are combined to determine the horizontal and vertical velocities under the assumption that ocean currents are horizontally uniform over the beam separations. Uncertainties of 3.2 cm s^{-1} in individual estimates are reduced by averaging in depth bins over many (120) pings. Even under ideal conditions—steady, horizontally uniform currents and zero instrument tilt—the response of a lowered ADCP is attenuated at high vertical wavenumbers. Sources of smoothing include finite acoustic transmission and reception intervals [section 4a(1)], first-differencing of the resulting velocity profiles [section 4a(2)], interpolation of the first-differenced profiles onto a regular depth grid [section 4a(3)], instrument tilt (section 4b), beam separation [section 4c(1)], instrument lowering [section 4c(2)], and package rotation (appendix B). The latter three issues require consideration of the ocean's horizontal wavenumber spectrum but produce relatively little attenuation. At each step, sampling and processing convolve the true velocity profile with either 1 or 2 boxcars so that the spectral response or transfer functions are products of sinc^2 functions [defined following (5)]. Finally, the effects of instrument attenuation on realistic broadband oceanic spectra are considered (section 4d) and the corrected LADCP spectra are compared with the XCP spectrum (section 4e).

a. The ideal lowered ADCP transfer function for horizontally uniform currents

We first consider the vertical smoothing caused by an ideal ADCP with no tilt, rotation, or lowering sampling a horizontally uniform flow.

1) RANGE AVERAGING

Even single-ping ADCP estimates of velocity are not point measurements but range averages over the lengths

of the transmitted sound pulse (projected on the vertical) $\Delta z_t = c\Delta t_t \sin\theta$ (=16 m for our 150-kHz measurements) and the depth bin Δz_r ($=c\Delta t_r \sin\theta = 16$ m set by the range gate of the received backscattered signal), where c is the speed of sound and $\theta = \pi/3 = 60°$ the beam angle with respect to the horizontal plane. Each averaging interval corresponds to a boxcar average of lengths Δz_t and Δz_r, respectively. The net effect is convolution of the true velocity profile with a trapezoid of length $\Delta z_t + \Delta z_r$. Letting $u(z)$ be the true water velocity profile with z positive upward, and u_{Pi} be translation motion of the instrument package, the single-ping relative velocity sampled during ping i in depth bin j centered on depth z_{ij} is

$$\mathring{u}_{ij} = \frac{1}{\Delta z_t \Delta z_r} \int_{-\Delta z_r/2}^{\Delta z_r/2} \int_{-\Delta z_t/2}^{\Delta z_t/2} [u(z_{ij} + \xi' + \xi'') - u_{Pi}]\, d\xi'\, d\xi''$$

$$= \mathcal{L}_{\text{ra}}\{u(z_{ij})\} - u_{Pi}, \tag{4}$$

where, for compactness, we have introduced the linear operator $\mathcal{L}_{\text{ra}}$ to represent the convolution of the velocity profile with the trapezoid due to the sonar's range averaging due to the finite bin and pulse lengths. The corresponding spectral transfer function in the vertical wavenumber domain is

$$T_{\text{ra}}(k_z) = \text{sinc}^2\left(\frac{k_z \Delta z_t}{2\pi}\right) \text{sinc}^2\left(\frac{k_z \Delta z_r}{2\pi}\right), \tag{5}$$

where $k_z = 2\pi/\lambda_z$ is the vertical wavenumber and $\text{sinc}(x) = \sin(\pi x)/(\pi x)$.

2) First-differencing

To eliminate unknown package motion u_{Pi}, the single-ping velocity profiles are first-differenced, yielding raw single-ping shear estimates

$$\mathring{u}_{zij} = \frac{\mathring{u}_{ij} - \mathring{u}_{ij+1}}{\Delta z_r} = \frac{1}{\Delta z_r} \int_{z_{ij}-\Delta z_r}^{z_{ij}} \frac{d(\mathcal{L}_{\text{ra}}\{u(z)\})}{dz}\, dz$$

$$= \frac{1}{\Delta z_r} \mathcal{L}_{\text{ra}} \left\{ \int_{-\Delta z_r/2}^{\Delta z_r/2} u_z\left(z_{ij} - \frac{\Delta z_r}{2} + \xi\right) d\xi \right\}$$

$$= \mathcal{L}_{\text{ra}} \left\{ \mathcal{L}_{\text{fd}} \left[u_z\left(z_{ij} - \frac{\Delta z_r}{2}\right) \right] \right\}, \tag{6}$$

where $u_z(z)$ is the true shear profile and $z_{ij} - \Delta z_r$ is the central depth of the single-ping shear estimate. First-differencing smooths the shear by convolution with a boxcar of length Δz_r (i.e., $\mathcal{L}_{\text{fd}}$). In the spectral domain, this corresponds to a transfer function

$$T_{\text{fd}}(k_z) = \text{sinc}^2\left(\frac{k_z \Delta z_{\text{fd}}}{2\pi}\right) \tag{7}$$

where Δz_{fd} is the vertical first-differencing interval. There is no advantage to choosing a finite-differencing interval other than the receive (bin) interval Δz_r since Δz_{fd} is necessarily greater than or equal to Δz_r and $\Delta z_{\text{fd}} > \Delta z_r$ would cause more smoothing.

3) Interpolation

The single-ping shear profiles are then linearly interpolated and averaged onto a uniform depth grid of interval Δz_g spanning the full water column. First, the single-ping shear profiles are made into piecewise-linear continuous profiles

$$\hat{u}_{z_i}(z) = \mathring{u}_{z_{ij+1}} + (\mathring{u}_{z_{ij+1}} - \mathring{u}_{z_{ij}}) \frac{z_{ij} - \Delta z_r/2 - z}{\Delta z_r}, \tag{8}$$

for $z_{ij} - \Delta z_r/2 \geq z \geq z_{ij} + \Delta z_r/2$. These are then bin averaged with depth to create a single shear profile spanning the depth range of the cast. Depth averaging the single-ping shears [(8)] in each depth grid interval Δz_g ($=z_{k+1} - z_k = 5$ m here) of the composite grid, then ensemble averaging over all pings contributing to depth interval k, yields the composite shear at interpolation grid point k

$$\langle \mathring{u}_{z_k} \rangle = \frac{1}{K\Delta z_g} \sum_{i=1}^{K} \int_{-\Delta z_g/2}^{\Delta z_g/2} \hat{u}_{z_i}(z_k + \xi)\, d\xi$$

$$= \frac{1}{K} \sum_{i=1}^{K} \mathcal{L}_{\Delta z_g}\{\hat{u}_{z_i}\}, \tag{9}$$

where i ranges over the $K \sim 120$ pings for which $\hat{u}_{z_i}$ is defined in $-\Delta z_g/2 \leq \xi \leq \Delta z_g/2$. The integral smooths with a boxcar of length Δz_g represented by the operator $\mathcal{L}_{\Delta z_g}\{\cdot\}$.

The summation over pings i in (9) can be replaced with an integral under the assumption that the discrete shear sample depths $z_{ij} - \Delta z_r/2$ uniformly span depth in the limit as $\Delta z_g \to 0$. It is necessary to define a continuous function $\tilde{u}_z(z)$, which matches the discrete shear estimates $u_{z_{ij}}$ at each $z = z_{ij} - \Delta z_r/2$, that is, a continuous analog to [(6)]

$$\tilde{u}_z(z) = \mathcal{L}_{\text{ra}}\{\mathcal{L}_{\text{fd}}\{u_z(z)\}\}. \tag{10}$$

Substituting $\tilde{u}_z(z)$ for $u_{z_{ij}}$ in (8), then substituting (8) into (9), replacing the sum in (9) with an integral and rearranging,

$$\overline{u}_{z_k} = \mathcal{L}_{\Delta z_g} \left\{ \frac{1}{\Delta z_r^2} \int_{-\Delta z_r/2}^{\Delta z_r/2} \left[\tilde{u}_z\left(z_k + \frac{\Delta z_r}{2} - \xi\right) + \tilde{u}_z\left(z_k - \frac{\Delta z_r}{2} + \xi\right) \right] \times \left(\frac{\Delta z_r}{2} + \xi\right) d\xi \right\}$$

$$= \mathcal{L}_{\Delta z_g}\{\mathcal{L}_{\text{int}}\{u_z(z)\}\}. \tag{11}$$

The $\mathcal{L}_{\text{int}}$ is a convolution by a triangle of width $2\Delta z_r$ or,

equivalently, by two successive boxcars of width Δz_r, represented by the linear operator

$$\mathcal{L}_{\rm int}\{u_z(z)\} = \frac{1}{\Delta z_r^2}\int_{-\Delta z_r/2}^{\Delta z_r/2}\int_{-\Delta z_r/2}^{\Delta z_r/2} u_z(z+\xi+\xi')\,d\xi\,d\xi'$$

with corresponding spectral transfer function

$$T_{\rm int}(k_z) = {\rm sinc}^4\left(\frac{k_z\Delta z_r}{2\pi}\right){\rm sinc}^2\left(\frac{k_z\Delta z_g}{2\pi}\right) \qquad (12)$$

for $k_z < 2\pi/\Delta z_r$, where ${\rm sinc}^2(k_z\Delta z_g/2\pi) \simeq 1$ to a good approximation over wavenumbers of interest since $\Delta z_r \gg \Delta z_g$. Provided data are randomly distributed throughout each depth bin, interpolating causes more smoothing than a simple depth-bin average, for which the smoothing is described by ${\rm sinc}^2(k_z\Delta z_r/2\pi)$.

b. Tilting

Instrument inclination, or tilt, will affect ADCP velocity estimates in vertically varying currents $u(z)$ because a line connecting the center of each range bin for a pair of opposing beams is then not horizontal (Fig. 2) resulting in relative depth offsets in range cells of opposing beams. In vertically varying currents, these depth offsets cause vertical smoothing when the opposing beams are combined to estimate horizontal velocity. The lowered ADCP has a tilt sensor so the effect of tilt can be evaluated (Fig. 3).

For a horizontally uniform velocity field with a sinusoidal vertical structure

$$u(z, k_z) = u_o e^{ik_z z}, \qquad (13)$$

the instrument response can be modeled as a sum of the velocities at the center of each depth cell z_o from opposing beams

$$u_{\rm ADCP}(z_o, k_z, D^+, D^-) = \frac{u_o}{2}[e^{ik_z(z_o-D^+)} + e^{ik_z(z_o-D^-)}], \qquad (14)$$

where $D^\pm$ represent the displacements due to tilting of the center of range cells from nominal depth $z = z_o = z_{\rm ADCP} - z'$ for the opposing ($\pm$) beams. For instrument tilts of $\Delta\theta$, and opposing beams oriented at angles ϕ and $\phi + \pi$ around the plane normal to the tilt axis (Fig. 2), the depth offsets are

$$D^\pm = r'\{-\sin\theta[1 - \cos(\Delta\theta)] \pm \cos\theta\sin(\Delta\theta)\sin\phi\}, \qquad (15)$$

where $r' = z'/\sin\theta$ is the slant range, $\theta = \pi/3$ the down-look angle, and the instrument is tilted about the x axis by $\Delta\theta$. For a beam lying in a plane normal to the tilt axis ($\phi = \pi/2$), a typical tilt of $\Delta\theta \sim 3°$ found in these data implies a displacement of $D^\pm = \pm 8$ m at the maximum vertical range of 270 m considered here. For such small tilts, $D^+ \simeq -D^-$, and the instrument response is

$$u_{\rm ADCP}(z_o, k_z, D) \simeq u_o e^{ik_z z_o}\cos(k_z D), \qquad (16)$$

where $D = (D^+ - D^-)/2 = r'\cos\theta\sin\phi\sin(\Delta\theta)$. The lowered ADCP produces an attenuated estimate of the velocity at z_o, which depends upon range, tilt, and orientation of the sensors with respect to the tilt axis. Displacements D and the resulting attenuation diminish with decreasing range, that is, as the instrument approaches depth z_o. Variable attenuation can also arise from variability in ϕ and $\Delta\theta$ during the measurement period but is not considered here.

A model for the instrument response to tilt can be constructed assuming both ϕ and $\Delta\theta$ are constant over the measurement interval and the lowering rate is uniform. Then, the expected value of the velocity estimate

$$\langle u_{\rm LADCP}(z_o, k_z|\Delta\theta, \phi)\rangle = u_o e^{ik_z z_o}\int \cos(k_z D){\rm pr}(D|\Delta\theta, \phi)\,dD, \qquad (17)$$

where "pr" is a probability distribution, reduces to

$$\langle u_{\rm LADCP}(z_o, k_z|\Delta\theta, \phi)\rangle = \frac{u_o e^{ik_z z_o}}{D^u_{\rm max} - D^u_{\rm min}}\int_{D^u_{\rm min}}^{D^u_{\rm max}}\cos(k_z D)\,dD = u_o e^{ik_z z_o}\,{\rm sinc}\left(\frac{kD^u_{\rm max}}{\pi}\right),$$

where $D^u_{\rm min/max} = r'_{\rm min/max}\cos\theta\sin\phi\sin(\Delta\theta)$. For the orthogonal pair of beams, $D^v_{\rm min/max} = r'_{\rm min/max}\cos\theta\sin(\phi + \pi)\sin(\Delta\theta)$. A tilt transfer function can then be defined

$$T_{\rm tilt}(k_z|\Delta\theta, \phi) = \frac{\langle u_{\rm LADCP}(z_o, k_z|\Delta\theta, \phi)\rangle\langle u_{\rm LADCP}(z_o, k_z|\Delta\theta, \phi)^*\rangle}{uu^* + vv^*} + \frac{\langle v_{\rm LADCP}(z_o, k_z|\Delta\theta, \phi)\rangle\langle v_{\rm LADCP}(z_o, k_z|\Delta\theta, \phi)^*\rangle}{uu^* + vv^*} \simeq \frac{{\rm sinc}^2\left(\frac{k_z D^u_{\rm max}}{\pi}\right) + {\rm sinc}^2\left(\frac{k_z D^v_{\rm max}}{\pi}\right)}{2}, \qquad (18)$$

which is the sum of two sinc^2 functions (of different low-pass characteristics in general). The average response can be expressed

$$T_{\rm tilt}(k_z) = \frac{1}{2\pi}\int_0^{2\pi} d\phi\int d\Delta\dot\theta\,{\rm pr}(\Delta\theta)T_{\rm tilt}(k_z|\Delta\theta, \phi), \qquad (19)$$

where probability distribution ${\rm pr}(\Delta\theta)$ is empirically defined from engineering data, and the instrument orientation ϕ is assumed independent of inclination $\Delta\theta$.

In practice, tilt attenuation is limited by the bin-mapping capabilities of the RDI (1996) processing. When D exceeds the range cell width Δz_r, RDI bin mapping calculates the velocity from those opposing range cells closest to the nominal vertical ranges; $D^u_{\rm max}$ and $D^v_{\rm max}$ can

be much larger than Δz_r if instrument tilts are substantial. The displacement D is therefore limited to values $D < \Delta z_r/2$. An appropriate transformation can be applied to the probability distribution $\mathrm{pr}(D|\Delta\theta, \phi)$ in (17) to reflect this bin mapping. In the limit of large $(r'_{\max} - r'_{\min})\cos\theta$, $\mathrm{pr}(D|\Delta\theta, \phi)$ will tend to a boxcar distribution with $\mathrm{pr}(D|\Delta\theta, \phi) = 1/\Delta z_r$ for $|D| < \Delta z_r/2$ and 0 otherwise. In this limit $T_{\mathrm{tilt}}(k_z)$ approaches $\mathrm{sinc}^2(k_z\Delta z_r/2\pi)$.

In order to obtain an estimate of the attenuation associated with instrument tilt with the RDI bin mapping enabled, the bin-mapping transformation was applied numerically to $\mathrm{pr}(D|\Delta\theta, \phi)$, (17) was evaluated for both pairs of beams, and the average response numerically estimated. Empirical fits to the resulting transfer functions $T_{\mathrm{tilt}}(k_z)$ give

$$T_{\mathrm{tilt}}(k_z) \simeq \mathrm{sinc}^2\left(\frac{k_z d'}{2\pi}\right) \tag{20}$$

for vertical wavenumbers $k_z < 0.2$ rad m^{-1} where, for minimum vertical range $z'_{\min} = r'_{\min}\sin\theta = 16$ m, $d' = 5.75$, 9.0, and 12.5 m for maximum vertical range $z'_{\max} = r'_{\max}\sin\theta = 96$, 160, and 272 m, respectively. Smoothing due to instrument tilt can be minimized by using bin mapping and short ranges. With bin mapping enabled, $d' < \Delta z_r$ even for long ranges. Thus, in general, attenuation will be less than $\mathrm{sinc}^2(k_z\Delta z_r/2\pi)$ so instrument tilts produce less smoothing than the previously discussed processes and the assumption that instrument orientation ϕ be independent of inclination $\Delta\theta$ is not critical.

c. *Vertical averaging of horizontally nonuniform currents*

The oceanic internal-wave field is not horizontally uniform. Variability on horizontal scales comparable to the spread of the acoustic beams $2x' = 2z'\cot\theta$ is associated with high-horizontal-wavenumber (high frequency) internal waves. Horizontal nonuniformity of the currents degrades the signal in several ways. First, the combination of slant velocities [(2)] will both smooth over horizontally varying horizontal velocities and be contaminated by horizontally nonuniform vertical velocities. These sources of signal degradation are considered for a stationary instrument in section 4c(1). Second, package motion through the water averages over varying phases of a horizontally variable field. Two models incorporating package motion are considered: lowering [section 4c(2)] and lowering with rotation (appendix B).

The beam-separation transfer function is the most difficult to evaluate, as well as the most uncertain, since it depends on the oceanic horizontal wavenumber spectrum, which is not well constrained by single lowered ADCP–CTD profiles. However, it also proves to have the least impact of the spectral transfer functions, contributing only a slight additional correction.

The effect of beam separation on the velocity estimate can be expressed as a function of internal-wave vertical wavenumber k_z and intrinsic frequency ω_i (because the horizontal structure of an internal wave is related to its vertical structure and intrinsic frequency through the dispersion relation). Isolated vertical profiles, such as those discussed here, contain contributions from a range of frequencies and wavenumbers. Defining a beam-separation transfer function solely in terms of vertical wavenumber, as appropriate for profile data, requires weighting the frequency/vertical wavenumber transfer function by a frequency spectrum and then integrating over frequency. However, the ocean frequency spectrum is not generally known in single profiles. In order to develop some intuition about the sensitivity of such transfer functions to frequency weighting, below we consider wave fields (i) described by a Garrett and Munk (GM) internal-wave model (Garrett and Munk 1975; Cairns and Williams 1976; Gregg and Kunze 1991) with varying near-inertial and near-buoyancy peaks, and (ii) composed only of semidiurnal internal tides.

1) BEAM-SEPARATION EFFECTS FOR A STATIONARY PACKAGE

A beam-separation model is constructed using the geometry of the ADCP measurement (Fig. 2). This involves evaluating the ADCP's estimate of the horizontal velocity [(2)] from a pair of opposing beams lying in the x, z plane at depth z as a function of the oceanic velocity field. The instrument is located at $(x, y, z) = (0, 0, z_o + z')$, where $z' = r'\sin\theta$ is the *vertical* range from the ADCP to the ensonified volumes at $(x, y, z) = (\pm z'\cot\theta, 0, z_o)$ and $\theta = 60°$ is the downlook angle. Ensonified volumes are assumed to be infinitesimally small since realistic beamwidths do not produce significant additional averaging (appendix A).

In order to quantify beam-separation effects, the oceanic velocity field is assumed to obey linear internal-wave kinematics. For a single linear plane wave, the velocity field in the x, z plane can be written

$$w = w_o \exp[i(k_x x + k_y y + k_z z - \omega t)]$$

$$u = -\frac{k_z}{k_h}\left(\cos\gamma + \frac{if\sin\gamma}{\omega}\right)w_o \times \exp[i(k_x x + k_y y + k_z z - \omega t)], \tag{21}$$

where $(k_x, k_y, k_z) = (k_h\cos\gamma, k_h\sin\gamma, k_z)$ is the wavevector, $k_h = \sqrt{k_x^2 + k_y^2}$ the horizontal wavenumber, $k_h^2/k_z^2 = (\omega^2 - f^2)/(N^2 - \omega^2)$the internal-wave dispersion relation, N the buoyancy frequency, f the Coriolis frequency, and ω the wave intrinsic frequency. Results are presented for an isotropic spectrum, which requires integration over the orientation of the horizontal wavevector, $\gamma = \arctan(k_y/k_x)$. From the measurement geometry

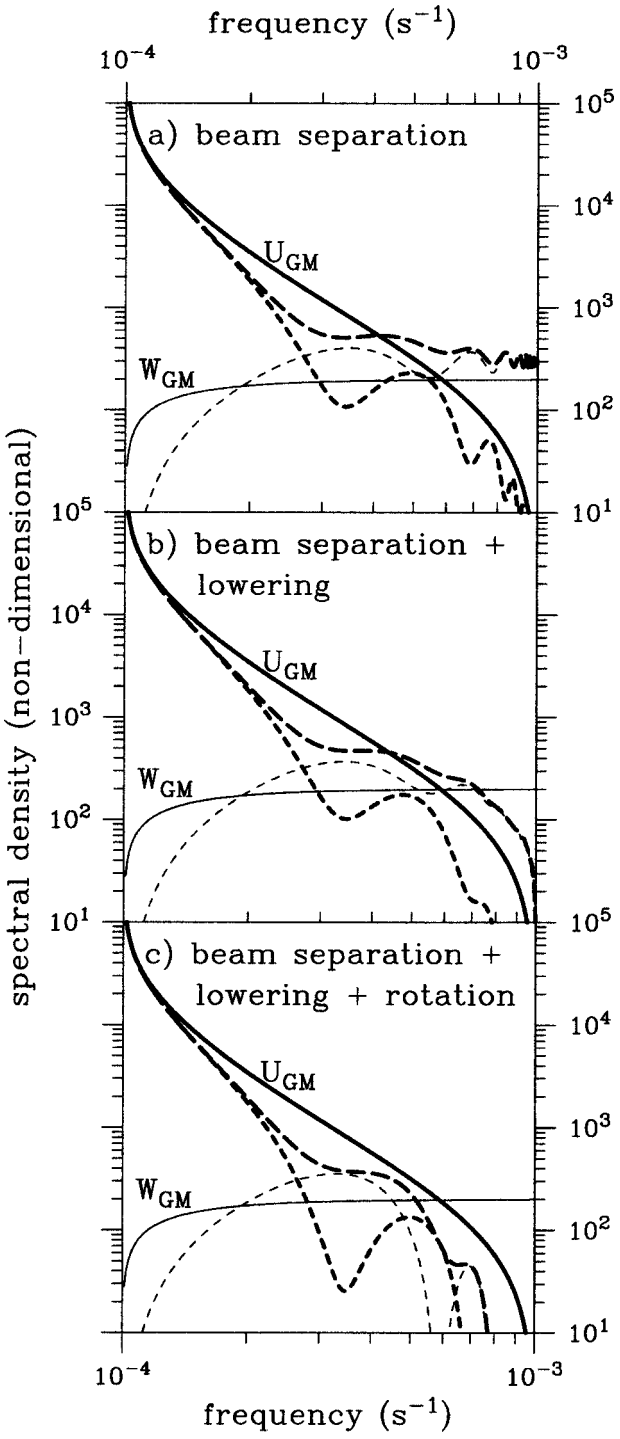

FIG. 8. The response of lowered ADCP beam-separation models as a function of internal-wave intrinsic frequency (0.74 days −1.75 h) at $\lambda_z = 100$ m in a GM wave field with $f = 10^{-4}$ rad s^{-1}, $N = 10^{-3}$ rad s^{-1}. The GM spectrum is depicted by solid curves (u thick, w thin), the instrument's interpretation of GM u and w spectra by short-dash curves, the total instrument response by the thick long-dash curve. (a) The stationary ADCP response associated with beam-separation alone [(23)], (b) includes the effects of lowering, and (c) lowering plus rotation [(B5)]. The depth range $z_1' = 150$ m in (23) for (a), while $z_1' = 100$ and $z_2' = 200$ m in (25) and (B5) for (b) and (c), respectively. The instrument response is a product of the transfer function and the GM spectra. Conversion between horizontal beam separation and horizontal wavenumber [i.e., the input arguments of (23)] is accomplished by specifying the depth ranges (z_1' and z_2') and the downlook angle θ. Conversion between horizontal wavenumber and wave frequency ω (horizontal axis) is accomplished by specifying the vertical wavelength λ_z and invoking the linear internal-wave dispersion relation.

[substituting (21) into (2)], the ADCP estimate of horizontal velocity is

$$
\begin{aligned}
u &= \frac{v_{\parallel}^{-} - v_{\parallel}^{+}}{2\cos\theta} \\
&= \frac{u(x^-) + w(x^-)\tan\theta + u(x^+) - w(x^+)\tan\theta}{2} \\
&= \frac{u}{2}[e^{ik_x x^+} + e^{-ik_x x^+}] - \frac{w}{2}[e^{ik_x x^+} - e^{-ik_x x^+}]\tan\theta \\
&= \left\{ -\frac{k_z}{k_h}\left(\cos\gamma + \frac{if\sin\gamma}{\omega}\right)\cos(k_h z'\cos\gamma\cot\theta) \right. \\
&\quad \left. - i\tan\theta\sin(k_h z'\cos\gamma\cot\theta)\right\} w_o \\
&\quad \times \exp[i(k_y y + k_z z - \omega t)]. \qquad (22)
\end{aligned}
$$

where $x^{\pm} = \pm z'\cot\theta$. For a *stationary* ADCP, provided the periods of high-frequency waves are long compared to the averaging interval, the beam-separation transfer function for an isotropic wave field is

$$
\begin{aligned}
&\tilde{T}_{\mathrm{bs}}(k_z, \omega, f, N, z_1) \\
&\quad = \frac{\int_0^{2\pi} u_{\mathrm{ADCP}} u_{\mathrm{ADCP}}^{*}\, d\gamma}{\int_0^{2\pi} uu^{*}\, d\gamma} \\
&\quad = \frac{1}{2} + \frac{J_1(2\psi)}{2} + \left[\frac{\omega^2 - f^2}{\omega^2 + f^2}\right]\frac{J_2(2\psi)}{2} \\
&\qquad - \frac{\omega^2(\omega^2 - f^2)\tan^2\theta[1 - J_0(2\psi)]}{(N^2 - \omega^2)(\omega^2 + f^2)}, \qquad (23)
\end{aligned}
$$

where the argument $2\psi = 2k_h z'\cot\theta$, J_n is an order-n Bessel function, and u_{ADCP} is given by (22). The first three terms denote the instrument's response to horizontal currents, the fourth the instrument's misinterpretation of horizontally nonuniform vertical velocities as horizontal currents. For the chosen vertical range z', buoyancy frequency N, Coriolis frequency f, and vertical wavenumber $k_z = 2\pi/\lambda_z$ (Fig. 8), the transfer function (23) exhibits a minimum at $k_h = 3.8/x' = 1.9/(z'\cot\theta)$ ($\omega = 3.4 \times 10^{-4}$ rad s^{-1}, Fig. 8) where $2x' = 2z'\cot\theta$ is the horizontal beam separation. For an anisotropic wave field perfectly aligned with the acoustic beams, a zero T_{bs} transfer func-

tion is anticipated when horizontal velocities at the two beams are 180° out of phase, that is, $k_h = \pi/(2z' \cot\theta)$ ($\omega = 2.9 \times 10^{-4}$ rad s^{-1}, Fig. 8). For the horizontally isotropic field assumed here, a minimum rather than zero occurs at a slightly higher wavenumber. For horizontal wavenumbers much higher than $\pi/(2z' \cot\theta)$, the horizontal velocities measured by the two beams are incoherent and the horizontal velocity contribution to the transfer function [(23)] tends to 1/2.

High-frequency internal-wave vertical velocities incoherent over the beam separation are misinterpreted as a horizontal velocity variance that is $k_h^2 \tan^2\theta/(2k_z^2)$ times larger than the oceanic horizontal velocity variance at that frequency [(23), Fig. 8]. However, at any given vertical wavelength, oceanic vertical velocities are typically an order of magnitude smaller than horizontal velocities so this is not generally a major source of error; Wijesekera et al. (1993) offer a counterexample over Yermak Plateau.

2) LOWERING

The lowered ADCP reduces random error in velocity estimates by averaging repeatedly sampled velocities at each depth. As the instrument approaches a given depth, beam separation diminishes. This accumulation of velocity estimates at depth z and variable horizontal range x' smooths over horizontally nonuniform currents

$$u_{\mathrm{LADCP}} = \frac{1}{\Delta z'} \int_{z_1'}^{z_2'} u_{\mathrm{ADCP}}(z')\, dz', \tag{24}$$

where z_1' and z_2' span the vertical range going into the estimate of u at depth z, $\Delta z' = z_2' - z_1'$, and u_{ADCP} is given by (22). The resulting transfer function for an isotropic wave field is

$$\tilde{T}_{\mathrm{bsl}}(k_z, \omega, f, N, z_1', z_2') = \frac{\displaystyle\int_0^{2\pi} u_{\mathrm{LADCP}} u_{\mathrm{LADCP}}^*\, d\gamma}{\displaystyle\int_0^{2\pi} uu^*\, d\gamma}, \tag{25}$$

where u for a plane internal wave is given by (21) and u_{LADCP} by (24). The integrand in the numerator is

$$\begin{aligned} u_{\mathrm{LADCP}} u_{\mathrm{LADCP}}^* = {} & \left\{ \underbrace{\left[\frac{N^2 - \omega^2}{\omega^2 - f^2}\right]\left(\cos^2\gamma + \frac{f^2 \sin^2\gamma}{\omega^2}\right) \mathrm{sinc}^2\left(\frac{k_o \Delta z'}{2\pi}\right) \cos^2(k_o \overline{z}')}_{\text{(i)}} - \underbrace{\tan^2\theta\, \mathrm{sinc}^2\left(\frac{k_o \Delta z'}{2\pi}\right) \sin^2(k_o \overline{z}')}_{\text{(ii)}} \right\} w_o^2 \\ & + \underbrace{\frac{2f}{\omega}\sqrt{\frac{N^2 - \omega^2}{\omega^2 - f^2}} \sin\gamma \tan\theta\, \mathrm{sinc}^2\left(\frac{k_o \Delta z'}{2\pi}\right)}_{\text{(iii)}} \cos(k_o \overline{z}') \sin(k_o \overline{z}'), \end{aligned} \tag{26}$$

where $k_o = k_x \cot\theta$ and $\overline{z}' = (z_1' + z_2')/2$. Term (i) represents the lowered ADCP's interpretation of the oceanic horizontal velocity, (ii) nonuniform vertical velocities being misinterpreted as horizontal velocities, and (iii) the cross product of u and w in an anisotropic internal-wave field propagating parallel to the plane of the two beams. Term (iii) is typically smaller than (i) or (ii), and vanishes in an isotropic wave field. Equation (25) is not analytically tractable and requires numerical integration over horizontal wave vector orientation γ for each (k_z, ω, f, N, z_1', z_2') of interest. However, it resembles (B5) for an isotropic wave field.

Horizontal smoothing by lowering dampens the high-frequency signal as the beams average over horizontal wavelengths smaller than the beam separation (Fig. 8). This can be seen by comparing the high-wavenumber response functions for stationary [(23)] and lowered [(25)] instruments (Fig. 8).

3) TRANSLATION

Averaging due to horizontal translations of water past the package will be relatively small away from regions of strong mean flow. For typical relative horizontal flows of 0.1 m s^{-1}, horizontal displacements are only 20 m over the 200 s it takes to sample over a depth range of 200 m. Such displacements are small compared to the 100 m swept over by each acoustic beam during lowering.

d. Lowered ADCP response in a broadband wave field

Instantaneous velocity profiles include contributions from all frequencies and horizontal wavenumbers. The response of the lowered ADCP to high horizontal wavenumbers (or equivalently high intrinsic frequencies through the dispersion relation) is biased because of beam-separation effects. In order to quantify this bias, the intrinsic frequency distribution of kinetic energy must be known. This is problematic for single profiles but, in principle, it can be accomplished by defining a vertical wavenumber transfer function

$$T_\omega(k_z) = \frac{\int_f^N \tilde{T}_{\mathrm{bsX}}(\omega, k_z) S[\mathrm{HKE}](\omega)\, d\omega}{\int_f^N S[\mathrm{HKE}](\omega)\, d\omega}, \quad (27)$$

where $\tilde{T}_{\mathrm{bsX}}(\omega, k_z)$ represents a beam-separation transfer function, such as (23) for a stationary ADCP or (B5) for lowering plus rotation, and $S[\mathrm{HKE}](\omega)$ is the internal-wave intrinsic frequency spectrum for horizontal kinetic energy. The problem then reduces to specifying the frequency spectrum $S[\mathrm{HKE}](\omega)$.

We wish to examine the sensitivity of the lowered ADCP estimate of horizontal velocity to the range of vertical and horizontal current structure found in the ocean. While the GM model (Garrett and Munk 1975; Cairns and Williams 1976; Gregg and Kunze 1991), most readily expressed in terms of intrinsic frequency ω and vertical wavenumber k_z, is a canonical description of the internal-wave field in the open ocean, it fails near rough topography and in large geostrophic currents. This motivates exploring model results using variants of the GM model frequency spectrum, and a wave field made up solely of ''semidiurnal'' waves.

The GM model frequency spectrum for vertical velocity has an unrealistic nonintegrable singularity at $\omega = N$. Modifying GM to have a variable but integrable vertical velocity peak as $\omega \to N$ and a variable inertial peak, the shape of the frequency spectrum for horizontal kinetic energy can be expressed as

$$S_{\mathrm{GM}}[\mathrm{HKE}](\omega) = \frac{f(\omega^2 + f^2)(N^2 - \omega^2)}{N^2\omega^4}\left(\frac{\omega^2}{\omega^2 - f^2}\right)^n\left(\frac{N^2}{N^2 - \omega^2}\right)^m \quad (28)$$

for $f < \omega < N$ where exponents n and m describe the strength of inertial and buoyancy peaks. Imposing limits on the exponents $n < 1$ and $m < 1$ ensures finite horizontal and vertical velocity variances. An inertial exponent $n = 1/2$ corresponds to the GM model and a buoyancy exponent $m = 0$ corresponds to a white vertical velocity spectrum as $\omega \to N$ as observed by D'Asaro and Lien (2000).

For the ''revised'' GM ($n = 1/2$, $m = 0$) wave field, transfer functions [(27)] including either the effects of lowering, or of lowering plus rotation [(B5)], agree closely with one another (Fig. 9). Package rotation does not introduce significant additional smoothing for a GM wave field because the additional averaging affects high frequencies much more than the near-inertial frequencies that dominate GM shear. The largest differences in Fig. 9 are between the stationary model [(23)], and models that account for package lowering [(25) and (B5)]. For wavelengths $\lambda_z > 100$ m, these differences are primarily due to the stationary instrument's greater sensitivity to horizontally nonuniform vertical velocities.

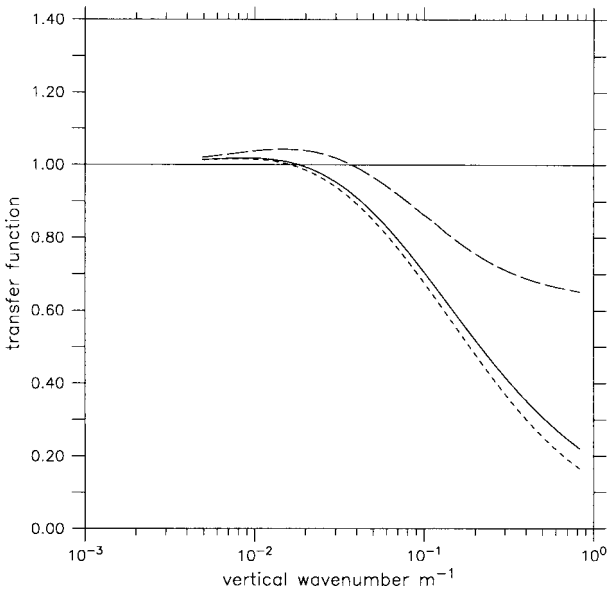

FIG. 9. Beam-separation transfer functions for a GM wave field. Curves depict model transfer functions for a stationary instrument (long-dash), with lowering (solid), and with lowering plus rotation (short-dash) using $N = 10^{-3}$ rad s^{-1}, $f = 10^{-4}$ rad s^{-1}, vertical ranges $z' = 144$ m for the stationary case, $z'_1 = 16$ m, and $z'_2 = 272$ m for the two lowered cases [(27) with (23), and (B5)]. Values greater than 1.0 at low wavenumber arise from misinterpretation of horizontally nonuniform vertical velocities as horizontal velocity.

A significant limitation of the above beam-separation model is the need to know the oceanic horizontal wavenumber (or intrinsic frequency) spectrum. Sensitivity of the response function to variability in the intrinsic frequency spectrum in the ocean is examined by (i) including an integrable singularity in the vertical velocity spectrum at $\omega = N$ [$m = 1/2$ in (28)], (ii) eliminating the inertial peak [$n = 0$ in (28)], and (iii) considering a wave field dominated by a single ''semidiurnal'' frequency $\omega = \sqrt{2}f$.

Model transfer function (27) is relatively insensitive to changes in the frequency weighting $S[\mathrm{HKE}](\omega)$ (Fig. 10). Sufficient averaging is associated with package motion that increasing horizontally nonuniform vertical velocities with an integrable singularity at $\omega = N$ does not alter the response. Together, the four frequency spectra weightings of (27) imply that, provided vertical shear is dominated by frequencies $\omega < 2f$ (a near-inertial peak), the model transfer function is not sensitive to the precise distribution of low-frequency shear and is well described by the GM results. However, if frequencies $\omega > 2f$ (e.g., a semidiurnal peak equatorward of 30°) dominate the shear, additional smoothing occurs and the instrument response is more variable (not shown).

While frequency spectra are not available from isolated lowered ADCP (LADCP) profiles collected during hydrographic surveys, past work has found that the shear/strain ratio R_ω can be used as a crude diagnostic of frequency content of the oceanic spectrum (Kunze et

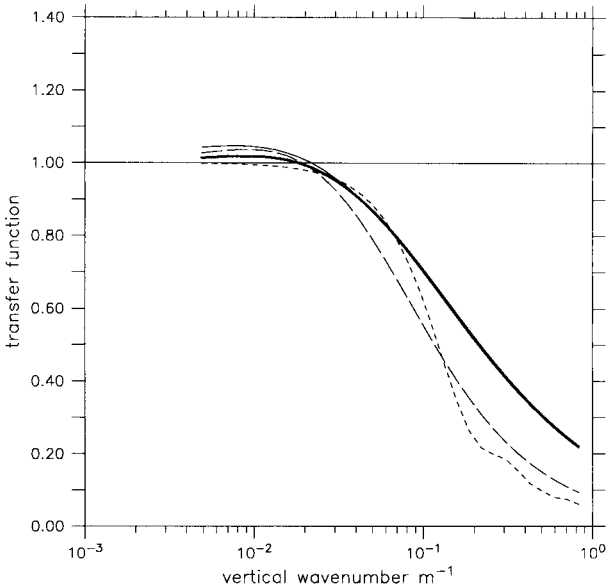

FIG. 10. Beam-separation transfer functions with lowering for ocean frequency spectra described by the GM model with a white vertical velocity spectrum (thick solid), with an integrable singularity at $\omega = N$ (thin solid), without an integrable singularity at $\omega = f$ (long-dash) and for an internal-wave field dominated by "semidiurnal" $\omega = \sqrt{2}f$ tides (short-dash) using $N = 10^{-3}$ rad s^{-1}, $f = 10^{-4}$ rad s^{-1}, $z_1' = 16$ m, and $z_2' = 272$ m. As in Fig. 9, values greater than 1.0 at low wavenumber arise from misinterpretation of horizontally nonuniform vertical velocities as horizontal velocity. The lowered transfer functions are insensitive to high-frequency vertical velocity (thick and thin solid) and are indistinguishable at high wavenumber.

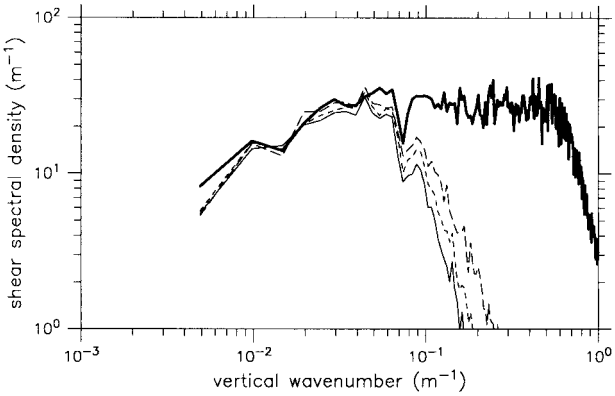

FIG. 11. Buoyancy-frequency-normalized shear V_z/N spectra vs vertical wavenumber k_z in rad m^{-1} from the XCP (thick solid), and LADCP using range bins 1–16 (thin solid), range bins 1–9 (short-dash), range bins 1–5 (long-dash). Spectra were smoothed with a 5-point triangular filter.

al. 1990; Polzin et al. 1995). Averaged over a single internal wave's phase, the shear/strain ratio

$$R_\omega = \frac{\langle V_z^2 \rangle}{N^2 \langle \xi_z^2 \rangle} = \frac{(N^2 - \omega^2)(\omega^2 + f^2)}{N^2(\omega^2 - f^2)}. \qquad (29)$$

Larger values of R_ω correspond to internal-wave fields weighted toward lower frequency. This diagnostic is not perfect as different frequency spectra can have the same shear/strain ratio, and it cannot distinguish frequencies in the continuum band, $f \ll \omega \ll N$. Contamination by subinertial finestructure is also a potential problem (Kunze 1993) although Polzin et al. (2002, manuscript submitted to *J. Phys. Oceanogr.*) suggest that these effects will be small for $\lambda_z > 50$ m. Nevertheless, one can infer whether an estimate of the beam-separation transfer function (27) employing a GM frequency spectrum (for which $R_\omega = 3$) adequately characterizes the smoothing. For shear/strain ratios greater than the GM value of 3 ($\omega \leq \sqrt{2}f$), little sensitivity is expected (<0.05) for $\lambda_z > 50$ m, with corrections smaller than those described above for $2 < R_\omega < 3$. For lower ratios ($R_\omega \leq 2$), as might arise from the absence of a near-inertial peak ($n = 0$) or dominance of semidiurnal shear equatorward of 30° latitude, much greater sensitivity is anticipated in the response functions so that beam-separation effects in lowered ADCP spectra cannot be as reliably quantified. Typically, shear/strain ratios in the ocean interior are 5–20 (Polzin et al. 1995).

In the dataset described here, shear/strain ratios are 5–6, near the 52° latitude semidiurnal ratio of 5. This ratio was calculated with the restriction that the θ, S relation be reasonably linear to minimize contamination by thermohaline fine structure.

e. Comparison of lowered ADCP and XCP in vertical wavenumber

Here, we determine that the model transfer functions described in sections 4a–4d account for the observed attenuation of small vertical scale fluctuations in the lowered ADCP (LADCP) profiles [(3), Fig. 7]. Principal uncertainties in this comparison are ill-defined noise contributions and a poorly constrained frequency spectrum for horizontal velocity. The range-dependent beam-separation response function (section 4c; appendix B) is the most model dependent. Spatial averaging associated with beam separation as well as instrument tilting can be minimized by using only range bins closest to the instrument to construct the shear profile estimate, but at a cost of higher noise levels because of less averaging.

With no correction for spatial averaging, the lowered ADCP and XCP spectra agree to within 10% for vertical wavelengths larger than 300 m (Figs. 11–12). At shorter wavelengths, the lowered ADCP spectrum rolls off with spectral attenuation more pronounced when longer ranges are included. This is consistent with either (i) reduced noise levels due to averaging over more pings, or (ii) more smoothing of the oceanic shear profile.

Correction of the lowered ADCP spectrum for the range-*independent* smoothing [(5), (7), and (12)] removes much of the discrepancy for vertical wavelengths larger than 50 m (Fig. 12). When the composite shear profile includes only ping data from shorter ranges, the

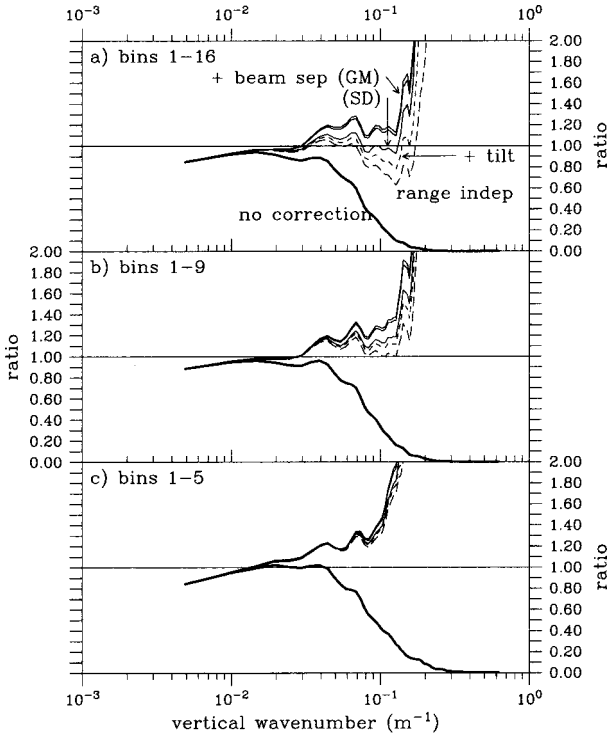

FIG. 12. Ratios between corrected LADCP and XCP spectra using range bins (a) 1–16, (b) 1–9, and (c) 1–5 where spectral transfer functions are $T_{\text{theo}}(k_z) = 1.0$ (thick solid; no correction);
$= T_{\text{ra}}(k_z)T_{\text{fd}}(k_z)T_{\text{int}}(k_z)$ (long-dash; range-independent smoothing only);
$= T_{\text{ra}}(k_z)T_{\text{fd}}(k_z)T_{\text{int}}(k_z)T_{\text{tilt}}(k_z)$ (short-dash; with tilt-induced smoothing); and
$= T_{\text{ra}}(k_z)T_{\text{fd}}(k_z)T_{\text{int}}(k_z)T_{\text{tilt}}(k_z)T_{\text{bs}}(k_z)$ (thin solid; with tilt and beam-separation-induced smoothing).
Only the last transfer function takes into account horizontal variability due to ocean internal waves. The four thin solid curves correspond to the two beam-separation models that account for package motion (lowering plus rotation) incorporating either a GM intrinsic frequency spectra or a semidiurnal (SD) frequency spike ($f = 1.15 \times 10^{-4}$ rad s^{-1}, $N = 1.7 \times 10^{-3}$ rad s^{-1}, bin size = 16 m). The GM spectrum contains more horizontal structure than the semidiurnal prescription. Consequently, the corrected spectra from the GM case are greater than those from the semidiurnal case. Little difference is noted (3% for GM, and none for semidiurnal at $\lambda_z > 50$ m) when package rotation is included in the beam-separation model.

corrected LADCP spectrum tends to *overestimate* the XCP spectrum due to instrument noise. Including data from longer ranges *underestimates* the XCP spectrum at vertical wavelengths larger than 50 m due to smoothing. Regardless of the range bins used to construct composite profiles, the corrected LADCP spectrum greatly exceeds the XCP spectrum at vertical wavelengths $\lambda_z < 50$ m due to instrument noise; lowered ADCP noise that is white in velocity [blue in shear as k_z^2] (Firing and Gordon 1990) dominates high wavenumbers. The presence of this noise is apparent in the corrected spectra as steeply rising levels at high wavenumbers (Fig. 12). Thus, it can be easily omitted from the finescale analysis described in section 5 by basing the spectral level estimate on wavenumbers below the noise's influence.

Compensation for range-*dependent* beam-separation effects requires specification of an intrinsic frequency spectrum. The observed shear/strain ratio $R_\omega = 5$–6 (21) is consistent with a dominant semidiurnal frequency, $\omega = 1.4 \times 10^{-4}$ rad s^{-1}. This frequency was used in a delta function specification of the spectrum, that is, semidiurnal waves only. Using data from all available range bins (1–16), the inclusion of range-dependent smoothing accounts for all but 10% of the discrepancy between the XCP and corrected LADCP spectra for vertical wavelengths longer than 50 m (Fig. 12). Using only range bins 1–5 eliminates range-dependent smoothing, but then the corrected LADCP exceeds the XCP spectra by as much as 40%. This is consistent with elevated noise levels due to averaging over fewer pings. There are thus trade-offs between using only shorter ranges to reduce beam-separation effects, or using more range bins at longer ranges to reduce noise. Since specifying the frequency spectrum in the manner described is somewhat uncertain, results are also shown assuming a GM frequency spectrum ($R_\omega = 3$). This degrades agreement between the corrected LADCP and XCP spectra using range bins 1–16. While the results depend on the frequency spectrum, we interpret the GM model results as an overcorrection given that the semidiurnal shear/strain ratio of 5–6 is higher than the GM value of 3. Finally, including instrument rotation in the beam-separation model did not change the results.

To summarize, we infer that (i) the ratio of corrected LADCP and XCP spectra tends to be closest to 1.0 when all available range bins are used to reduce random noise, (ii) since the oceanic shear spectrum is white, noise in the lowered ADCP estimate can be diagnosed by the occurrence of steeply rising blue spectra at high wavenumbers in the corrected spectra, and (iii) regardless of which range bins are used, instrument rotation does not produce significantly more averaging than lowering alone.

f. Model summary

In summary, the best transfer function describing the lowered ADCP's response for the above dataset takes into account range averaging (ra), finite differencing (fd), interpolation (int), instrument tilting (tilt), and beam separation with instrument lowering (bsl)

$$T_{\text{theo}}(k_z) = T_{\text{ra}}(k_z)T_{\text{fd}}(k_z)T_{\text{int}}(k_z)T_{\text{tilt}}(k_z)T_{\text{bsl}}(k_z)$$
$$= \text{sinc}^2\left(\frac{k_z\Delta z_t}{2\pi}\right)\text{sinc}^8\left(\frac{k_z\Delta z_r}{2\pi}\right)\text{sinc}^2\left(\frac{k_z\Delta z_g}{2\pi}\right)$$
$$\times\ \text{sinc}^2\left(\frac{k_z d'}{2\pi}\right)T_{\text{bsl}}(k_z), \qquad (30)$$

where $\Delta z_t = \Delta z_r = 16$ m, $\Delta z_g = 5$ m, and tilt-induced smoothing d' depends on range [(20)]. This compares favorably with the observed transfer function [(3), Fig. 7]. The $\text{sinc}^2(k_z\Delta z_g/2\pi)$ that arises from interpolation

[(12)] can be ignored here because $\Delta z_r \gg \Delta z_g$. Range-independent transfer functions for range-averaging $T_{ra}(k_z)$ [(5)] and finite-differencing $T_{fd}(k_z)$ [(7)] are well constrained. The tilt transfer function $T_{tilt}(k_z)$ [(20)] assumes that instrument inclination and heading statistics are invariant over the time it takes to sample a particular depth. The beam-separation transfer function with lowering is described by

$$T_{bsl}(k_z) = \frac{\int_f^N \tilde{T}_{bsl}(k_z, \omega, f, N, z_1', z_2') S[\mathrm{HKE}](\omega)\, d\omega}{\int_f^N S[\mathrm{HKE}](\omega)\, d\omega}, \tag{31}$$

where $\tilde{T}_{bsl}(k_z, \omega \ldots)$ must be calculated numerically [(27) with (28); see also (B5)]. This is the least-constrained of the transfer functions because of its sensitivity to (i) the horizontal wavenumber (or intrinsic frequency) spectrum for horizontal velocity $S[\mathrm{HKE}](\omega)$, which is not well known from single-profile measurements, and (ii) unknown anisotropy in the wave field.

If estimates of strain are not contaminated by permanent fine structure (Polzin et al. 2002, manuscript submitted to *J. Phys. Oceanogr.*), one can use the shear/strain ratio (29) to estimate the frequency content of the wave field, then use this to characterize the frequency weighting in (31). Alternatively, beam-separation effects can be ignored by setting $T_{bsl}(k_z) = 1.0$. This will bias finescale shears slightly low. Beam-separation effects can be reduced by using only shorter ranges (at the cost of increased noise), or by limiting analysis to longer wavelengths.

These results suggest the following steps to optimize the finescale response of a lowered ADCP. Using $\Delta z_r = \Delta z_t/2$ would be a great improvement because of the strong dependence on Δz_r in (30). This should not impact range or largescale accuracy. Smoothing due to instrument tilt and beam spreading can be minimized by using only short ranges. However, this comes at a cost of higher noise levels because fewer pings will then go into the average. Higher-frequency ADCPs would provide the same number of pings at reduced range.

5. Inferring eddy diffusivities

While it is valuable to have a better understanding of the lowered ADCP's finescale response for its own sake, there is considerable interest and oceanographic merit in using corrected LADCP spectra to infer diapycnal turbulent eddy diffusivities K. Accounting for spatial averaging, lowered ADCP profiles can provide shear spectra uncertain to within 20% for vertical wavelengths $\lambda_z > 50$ m. This implies 50% uncertainties in the estimates of the spectral level squared, which is used in finescale parameterizations for the turbulent dissipation rate

$$\varepsilon = \varepsilon_0 \frac{N^2}{N_0^2} \frac{\langle V_z^2 \rangle^2}{\langle \mathrm{GM} V_z^2 \rangle^2} f(R_\omega) \tag{32}$$

with $\varepsilon_0 = 7.8 \times 10^{-10}$ W kg^{-1} and $N_0 = 5.2 \times 10^{-3}$ rad s^{-1} (Gregg 1989; Polzin et al. 1995; Sun and Kunze 1999), themselves uncertain to within a factor of 2, provided that (i) the internal-wave frequency spectral shape does not deviate too markedly from the GM model and (ii) 10–12 independent realizations go into the estimate (Polzin et al. 1995); Gregg et al. (1993a) also noted that 10–12 realizations were needed to obtain factor of two uncertainties using microstructure measurements. There should therefore be a factor of 3–4 uncertainty in inferring the dissipation rate ε from corrected LADCP profiles. The shear/strain ratio (29) provides a crude means of assessing requirement (i) that the internal-wave frequency spectrum not differ too much from the GM model. The shear-only parameterization of Gregg (1989) [$f(R_\omega)$ set to one in (32)] was found to fall short of microstructure dissipation rates over the Yermak Plateau where internal tides and high-frequency bursts dominate the internal wave field (Wijesekera et al. 1993). Polzin et al. (1995) indicate that the shear/strain ratio correction $f(R_\omega)$ brought the fine- and microscale estimates into better agreement. Finescale parameterization [(32)] underestimated direct microstructure measurements of dissipation rate by a factor of 30 in Monterey Submarine Canyon (Kunze et al. 2002). The authors suggest that this may be due to interactions with topography, internal bores or solitary waves. The shear/strain ratio is close to and often less than one in Monterey Canyon.

Additional uncertainties arise in inferring eddy diffusivities K from the Osborn (1980) relation

$$K = \frac{\gamma \varepsilon}{N^2} = K_0 \frac{\langle V_z^2 \rangle^2}{\langle \mathrm{GM} V_z^2 \rangle^2} f(R_\omega), \tag{33}$$

with $K_0 \leq 0.05 \times 10^{-4}$ m^2 s^{-1} because of uncertainty in the mixing efficiency γ ($\leq$0.2 on energetic grounds). The mixing efficiency is usually set at its maximum value of $\gamma = 0.2$ by the microstructure community as appropriate for high-Reynolds-number turbulence in stratified (buoyancy frequency N *not* much less than the vertical shear V_z) waters.

As an example of this application, Fig. 13 compares inferred turbulent diffusivities K from each LADCP/XCP pair using the Gregg (1989) finescale parameterization for turbulent dissipation rate [(32) with $f(R_\omega) = 1$] and the Osborn (1980) relationship for turbulent diapycnal diffusivities (33) with mixing efficiency $\gamma = 0.2$. The GM76 model spectrum (Cairns and Williams 1976; Gregg and Kunze 1991) is used to estimate the GM variances. From the above discussion, factors of 3–4 uncertainty in lowered ADCP eddy diffusivity estimates are expected. This is sufficient to identify the hotspots that must be at least 2–3 orders of magnitude larger than typical open-ocean values (10^{-5} m^2 s^{-1}) if they are to account for basin averages of 10^{-4} m^2 s^{-1}.

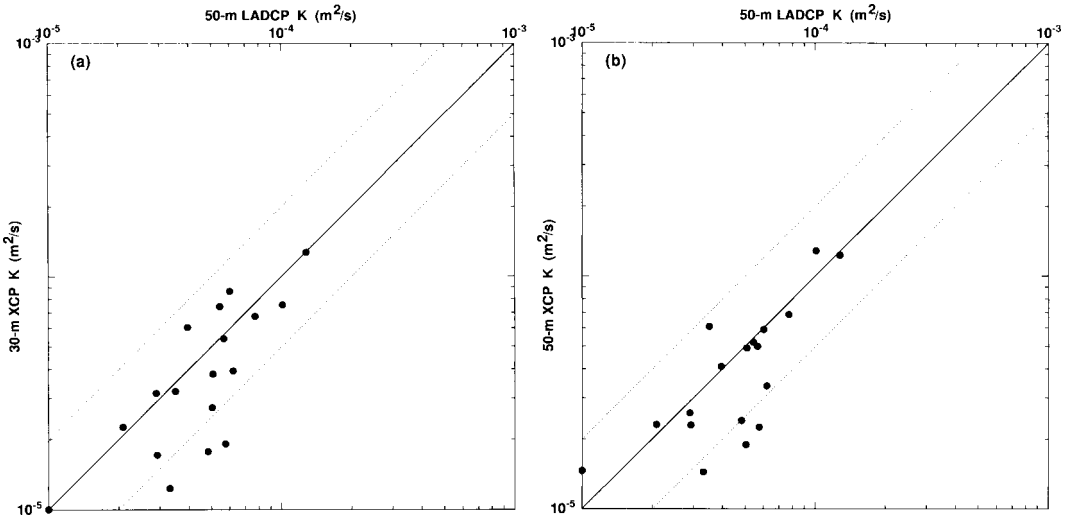

FIG. 13. Scatterplots of inferred turbulent diapycnal diffusivities K for each profile pair. (a) Eddy diffusivities based on lowered ADCP shear variances in vertical wavelengths $\lambda_z > 50$ m normalized by GM are compared to those from 30-m normalized XCP shear variances. (b) 50-m lowered ADCP diffusivities are compared with 50-m XCP diffusivities. The 50-m diffusivities are in reasonable agreement, the lowered ADCP values only slightly high. The 50-m diffusivities tend to overestimate 30-m inferred values and be more scattered but still lie within a factor of 2.

To obtain shear variances $\langle V_z^2 \rangle$, lowered ADCP shear spectra were computed from 64-point (1280 m) profile segments. These spectra were spectrally corrected using the observed transfer function (3), then integrated to a vertical wavenumber $k_z = 0.125$ rad m^{-1} ($\lambda_z = 50$ m). XCP shear spectra were integrated to $k_z = 0.2$ rad m^{-1} ($\lambda_z = 30$ m, Fig. 13a) or 0.125 rad m^{-1} ($\lambda_z = 50$ m, Fig. 13b). In all cases, the normalizing GM shear variances were integrated over the same wavenumber band as the observed variances. We caution that estimating the turbulent eddy diffusivity using (32) and (33) requires quantifying the spectral level for shear variance at wavenumbers lower than the cutoff where the spectral slope changes from flat to k_z^{-1} ($k_c = 0.6$ rad m^{-1} for the GM spectral level). If the turbulence and internal waves are elevated, there is evidence that the cutoff wavenumber decreases (Smith et al. 1987; Duda and Cox 1989; Gregg et al. 1993b) as $\langle V_z^2 \rangle k_c = $ constant. For example, eddy diffusivities of 10^{-2} m^2 s^{-1}, or 1000 times GM values, would imply internal wave spectral levels and cutoff wavelengths 30 times GM ($\lambda_c = 300$ m) so that longer profile segments are needed to reliably estimate the spectral level below the cutoff.

Lowered ADCP and XCP inferred diffusivities compare favorably. The 50-m inferred diffusivities have a greater tendency to be identical with some exceptions that lie about a factor of 2 apart. The 50-m lowered ADCP diffusivities tend to be larger than the 30-m XCP diffusivities but still lie within a factor of 2. Diffusivities lie between 10^{-5} and 10^{-4} m^2 s^{-1}, higher than found in the midlatitude pycnocline (Gregg 1989; Ledwell et al. 1993). Inferred kinetic energy turbulent dissipation rates ε lie between 2×10^{-10} and 2×10^{-9} W kg^{-1} (not shown), similar to typical midlatitude values (8×10^{-10} W kg^{-1}). Buoyancy fluxes $\langle w'b' \rangle = -\gamma\varepsilon$ will likewise be comparable. However, the buoyancy frequency $\overline{N} = 1.7 \times 10^{-3}$ rad s^{-1} is lower than found at similar depths at midlatitude, so diffusivities are higher [(33)]. Similarly enhanced diffusivities were inferred in the weakly stratified Southern Ocean near 55°S, 84°E (Polzin and Firing 1997) where vertically integrated dissipation rates were comparable to midlatitude values.

6. Summary

Lowered ADCP (LADCP) shear profiles were compared with 18 simultaneous higher-resolution XCP profiles to determine how well lowered ADCP measurements resolve finescale shear. The lowered ADCP spectra were found to be attenuated for wavelengths $\lambda_z < 150$ m (Fig. 5), and down by an order of magnitude at $\lambda_z = 50$ m. However, XCP and ADCP signals remained coherent to $\lambda_z = 50$ m (Fig. 6). Model transfer functions for spatial smoothing inherent in the ADCP processing [section 4, (30)] accounted for the observed attenuation to within ±20% (Figs. 7 and 12). The model transfer function accounts for vertical smoothing due to range averaging by the transmitted and received pulses [(5)], finite differencing [(7)], interpolation [(12)], instrument tilting [(20)], and horizontal smoothing due to beam separation [(23)] and lowering [(27) with (24) and (28)].

The greatest smoothing in these profiles is associated with range averaging (5). It could be substantially reduced by employing a shorter receive interval, for example, $\Delta z_r = \Delta z_t/2$ without detrimental effects on range or large-scale accuracy. Smoothing associated with tilt and beam-separation effects can be reduced by using only range bins closest to the instrument at the cost of

higher noise levels since fewer data points will then go into the averaging. The trade-offs between using shorter ranges to reduce beam-separation effects or using more range bins at longer ranges to reduce noise could be obviated in future measurements by using higher-frequency ADCPs, which collect the same number of pings over shorter ranges, though recent field experience by E. Firing indicates that this drastically reduces low-wavenumber accuracy.

For internal-wave frequency spectral shapes described by the GM model (Garrett and Munk 1975; Cairns and Williams 1976; Gregg and Kunze 1991), finescale shear variance can be used to infer the turbulent dissipation rate ε and diapycnal eddy diffusivity K due to internal wave breaking to within a factor of two (Gregg 1989). For weakly non-GM frequency spectra, a modification of the parameterization that incorporates finescale strain as well as shear variance has proven consistent with microstructure measurements to within a factor of two (Polzin et al. 1995; Sun and Kunze 1999). Thus, full-depth lowered ADCP profiles collected on hydrographic lines can be used to infer turbulence to perhaps within a factor of 3–4 over a variety of topographic and flow regimes.

When spectrally corrected LADCP data were used in the finescale parameterization of Gregg (1989), turbulent eddy diffusivities were within a factor of two of estimates based on higher-resolution XCP data (Fig. 13). Other considerations suggest that turbulence levels and eddy diffusivities can be inferred to within factors of 3–4 from lowered ADCP profiles. While the resulting diffusivity estimates may not be as accurate as microstructure measurements, existing data provide access to regions of the ocean unlikely to be sampled with microstructure sensors in the immediate future, and may help site future micro- and fine structure experiments. The factors of 3–4 uncertainties should not be an obstacle to locating localized hotspots, which must be at least 2–3 orders of magnitude higher that typical ocean interior values in order to close large-scale budgets.

Acknowledgments. This research was supported by NSF Grant OCE 97-27701. We thank Kathy Donohue for her assistance in deploying the XCPs, John Dunlap for processing the XCP data, Steve Anderson for insightful discussions regarding models of ADCP response, and Matthew Alford, Jim Ledwell, and an anonymous reviewer for comments on the manuscript.

APPENDIX A

Finite Beamwidth

Spatial averaging associated with a finite acoustic beamwidth has transfer function

$$T_{\rm bw}(k_z) = \frac{u_{\rm LADCP}(z_o)u_{\rm LADCP}(z_o)^*}{T_{ra}(k_z)u(z_o)u(z_o)^*} \tag{A1}$$

for horizontally uniform currents, where the instrument response is given by

$$u_{\rm LADCP}(z_o, k_z, \omega) = \frac{1}{2\pi}\frac{\displaystyle\int_{-\pi}^{\pi}\int_{-\pi/2}^{\pi/2}\int_0^{\infty} u(r', \theta', \phi)f(r')g(\theta')\,dr'\,d\theta'\,d\phi}{\displaystyle\int_{-\pi/2}^{\pi/2} g(\theta')\,d\theta'}, \tag{A2}$$

$z_o = z_{\rm ADCP} - z'$ is the depth of the velocity estimate, r' the slant range, the range cell weight function (RDI 1996)

$$f(r') = \begin{cases} 1 - \dfrac{|r' - \overline{r}'|}{\Delta r'} & \text{for } |r' - \overline{r}'| < \Delta r' \\ 0 & \text{for } |r' - \overline{r}'| > \Delta r', \end{cases} \tag{A3}$$

where $\overline{r}'$ is the midpoint of a range bin of width $\Delta r'$, the two-way beam-spread pattern is

$$g(\theta) = \left[\frac{2J_1(k_a a \sin\theta')}{k_a a \sin\theta'}\right]^4 \tag{A4}$$

from the theoretical response for a circular plane transducer (Urick 1967), $k_a = 643$ rad m^{-1} ($\lambda_a = 1$ cm) the wavenumber of the acoustic signal, $a = 0.0826$ m the radius of the transducer, coordinates (r', θ', ϕ) the slant range, polar angle, and azimuthal angle after rotating Cartesian coordinates displayed in Fig. 2 by $-5\pi/6$ about the y axis so that the z' axis is aligned with a beam, and expressing u in spherical polar coordinates, and J_1 an order-one Bessel function. The oceanic velocity field is assumed to be of the form (13), that is, $u = u_o e^{ik_z z}$. After integrating (A2) over ϕ analytically, and over r' and θ' numerically, even for vertical ranges $z' = r' \sin\theta$ as large as 260 m and vertical wavenumbers as high as $k_z = 0.6$ rad m^{-1}, $T_{\rm bw}(k_z) = 1.0 \pm 0.04$ [(A1)] because the half-power point for the two-way beam-spread pattern is only $\pm 1°$ from (A4), corresponding to vertical spreading of only ± 3 m at a vertical range of 260 m. This is smaller than the ± 5-m half-power point for the depth cell weight function. Smoothing associated with finite beamwidth would be of more concern at higher vertical wavenumber if smaller depth bins were used.

APPENDIX B

Lowering with Rotation

The CTD package tends to rotate by 0–$2\pi/50$ rad m^{-1} as it is lowered due to unwinding of the conducting cable or hydrodynamic torques on the package. When horizontal projections of the depth cells are considered, rotation rates of $2\pi/100$ rad m^{-1} ensonify an area that

can be described as a washer of inner radius $z_1' \cot\theta$ and outer radius $z_2' \cot\theta$, where z_1' and z_2' are the minimum and maximum vertical ranges sampling depth z. Here, lowering with rotation is modeled by averaging over the area of this washer. We consider this an upper bound on the averaging of horizontally nonuniform currents.

We introduce an arbitrary positive counterclockwise geographic heading α of the χ^+ acoustic beam relative to geographic east. The ADCP estimate of the east velocity u at vertical range z' is

$$\begin{aligned} u_{\mathrm{ADCP}}(z') = & \frac{[u(\chi^+) + u(\chi^-)]\cos^2\alpha}{2} \\ & + \frac{[v(\chi^+) + v(\chi^-)\sin\alpha\cos\alpha}{2} \\ & - \frac{[w(\chi^+) - w(\chi^-)]\tan\theta\cos\alpha}{2} \\ & + \frac{[u(\eta^+) + u(\eta^-)]\sin^2\alpha}{2} \\ & - \frac{[v(\eta^+) + v(\eta^-)]\sin\alpha\cos\alpha}{2} \\ & + \frac{[w(\eta^+) - w(\eta^-)]\tan\theta\sin\alpha}{2} \end{aligned} \quad \text{(B1)}$$

in beam coordinates

$$\begin{aligned} \chi^{\pm} &= (\pm z' \cot\theta \cos\alpha, \pm z' \cot\theta \sin\alpha, z) \\ \eta^{\pm} &= (\mp z' \cot\theta \sin\alpha, \pm z' \cot\theta \cos\alpha, z), \end{aligned} \quad \text{(B2)}$$

where the ocean velocities are

$$\begin{aligned} w &= w_o \exp[i(k_x x + k_y y + k_z z - \omega t)] \\ u &= -\frac{k_z}{k_h}\left(\cos\gamma + \frac{if\sin\gamma}{\omega}\right) w_o \\ &\quad \times \exp[i(k_x x + k_y y + k_z z - \omega t)] \\ v &= -\frac{k_z}{k_h}\left(\sin\gamma - \frac{if\cos\gamma}{\omega}\right) w_o \\ &\quad \times \exp[i(k_x x + k_y y + k_z z - \omega t)]. \end{aligned} \quad \text{(B3)}$$

The smoothed LADCP estimate of the zonal velocity is

$$u_{\mathrm{LADCP}}(z) = \frac{1}{2\pi\Delta r}\int_{z_1'}^{z_2'}\int_{-\pi}^{\pi} u_{\mathrm{ADCP}}(z')\, d\alpha\, dz'. \quad \text{(B4)}$$

For an isotropic wave field, the transfer function is

$$\begin{aligned} &\tilde{T}_{\mathrm{bsw}}(k_z, \omega, f, N, z_1', z_2') \\ &= \frac{\displaystyle\int_0^{2\pi} u_{\mathrm{LADCP}} u^*_{\mathrm{LADCP}}\, d\gamma}{\displaystyle\int_0^{2\pi} uu^*\, d\gamma} \\ &= \frac{4}{\Delta\psi^2}\Bigg([J_1(\psi_2) - J_1(\psi_1)]^2 \\ &\quad + \frac{4f^2}{(\omega^2 + f^2)}[J_1(\psi_2) - J_1(\psi_1)] \\ &\quad \times \sum_{k=1}^{\infty}[J_{2k+1}(\psi_2) - J_{2k+1}(\psi_1)] \\ &\quad + \frac{4f^2}{(\omega^2 + f^2)}\left\{\sum_{k=1}^{\infty}[J_{2k+1}(\psi_2) - J_{2k+1}(\psi_1)]\right\}^2 \\ &\quad + \frac{\omega^2(\omega^2 - f^2)}{(N^2 - \omega^2)(\omega^2 + f^2)} \\ &\quad \times \tan^2\theta[J_0(\psi_2) - J_0(\psi_1)]^2\Bigg), \end{aligned} \quad \text{(B5)}$$

where $\psi_i = k_h z_i' \cot\theta$ and $\Delta\psi = \psi_2 - \psi_1$.

Rapid rotation increases averaging of high-frequency motions. Rotation increases the depth of the first relative minimum in the lowered ADCP's response to horizontal velocity as well as attenuating higher frequency motions (Fig. 8).

REFERENCES

Althaus, A. M., E. Kunze, and T. B. Sanford, 1999: Internal tide generation and associated energy-flux near Mendocino Escarpment. *Eos, Trans. Amer. Geophys. Union,* **80,** 87.

Beal, L. M., and H. L. Bryden, 1997: Observations of an Agulhas Undercurrent. *Deep-Sea Res.,* **44,** 1715–1724.

Cairns, J. L., and G. O. Williams, 1976: Internal wave observations from a midwater float, Part 2. *J. Geophys. Res.,* **81,** 1943–1950.

Chapman, P., 1998: World Ocean Circulation Experiment generates wealth of data. *Eos, Trans. Amer. Geophys. Union,* **79,** 385–389.

D'Asaro, E. A., and R.-C. Lien, 2000: The wave–turbulence transition for stratified flows. *J. Phys. Oceanogr.,* **30,** 1669–1678.

Duda, T. F., and C. S. Cox, 1989: Vertical wavenumber spectra of velocity and shear at small internal wave scales. *J. Geophys. Res.,* **94,** 939–950.

Eriksen, C. C., 1998: Internal wave reflection and mixing at Fieberling Guyot. *J. Geophys. Res.,* **103,** 2977–2994.

Firing, E., and R. Gordon, 1990: Deep ocean acoustic Doppler profiling. *Proc. IEEE Fourth Working Conf. on Current Measurements,* Clinton, MD, Current Measurement Technology Committee of the Ocean Engineering Society, 192–201.

——, S. E. Wijffels, and P. Hacker, 1998: Equatorial subthermocline currents across the Pacific. *J. Geophys. Res.,* **103,** 21 413–21 423.

Fischer, J., and M. Visbeck, 1993: Deep velocity profiling with self-contained ADCPs. *J. Atmos. Oceanic Technol.,* **10,** 764–773.

——, F. Schott, and L. Stramma, 1996: Currents and transports of the Great Whirl–Socotra Gyre system during the summer monsoon, August 1993. *J. Geophys. Res.,* **101,** 3573–3587.

Garrett, C. J. R., and W. H. Munk, 1975: Space–time scales of internal waves: A progress report. *J. Geophys. Res.,* **80,** 291–297.

Gregg, M. C., 1989: Scaling turbulent dissipation in the thermocline. *J. Geophys. Res.,* **94,** 9686–9698.

——, and E. Kunze, 1991: Shear and strain in Santa Monica basin. *J. Geophys. Res.,* **96,** 16 709–16 719.

——, H. E. Seim, and D. B. Percival, 1993a: Statistics of shear and turbulent dissipation profiles in random internal wave fields. *J. Phys. Oceanogr.,* **23,** 1777–1799.

——, D. P. Winkel, and T. B. Sanford, 1993b: Varieties of fully resolved spectra of vertical shear. *J. Phys. Oceanogr.,* **23,** 124–141.

Hacker, P., E. Firing, W. D. Wilson, and R. Molinari, 1996: Direct observations of the current structure east of the Bahamas. *Geophys. Res. Lett.,* **23,** 1127–1130.

Hinrichsen, H. H., and A. Lehmann, 1994: A comparison of geostrophic velocities and profiling ADCP measurements in the Iberian Basin. *J. Atmos. Oceanic Technol.,* **11,** 901–914.

Hogg, N., P. Biscaye, W. Gardner, and W. J. Schmitz Jr., 1982: On the transport and modification of Antarctic Bottom Water in the Vema Channel. *J. Mar. Res.,* **40** (Suppl.), 231–263.

Hufford, G. E., M. S. McCartney, and K. A. Donahue, 1997: Northern boundary currents and adjacent recirculations off southwestern Australia. *Geophys. Res. Lett.,* **24,** 2797–2800.

Kunze, E., 1993: Submesoscale dynamics near a seamount. Part II: The partition of energy between internal waves and geostrophy. *J. Phys. Oceanogr.,* **23,** 2589–2601.

——, and T. B. Sanford, 1996: Abyssal mixing: Where it is not. *J. Phys. Oceanogr.,* **26,** 2286–2296.

——, and J. M. Toole, 1997: Tidally driven vorticity, diurnal shear and turbulence atop Fieberling Seamount. *J. Phys. Oceanogr.,* **27,** 2663–2693.

——, M. G. Briscoe, and A. J. Williams, 1990: Interpreting shear and strain finestructure from a neutrally-bouyant float. *J. Geophys. Res.,* **95,** 18 111–18 125.

——, L. K. Rosenfeld, G. S. Carter, and M. C. Gregg, 2002: Internal waves in Monterey Submarine Canyon. *J. Phys. Oceanogr.,* in press.

Ledwell, J. R., A. J. Watson, and C. S. Law, 1993: Evidence of slow mixing across the pycnocline from an open-ocean tracer-release experiment. *Nature,* **364,** 701–703.

Lueck, R. G., and T. D. Mudge, 1997: Topographically-induced mixing around a shallow seamount. *Science,* **276,** 1831–1833.

Marotzke, J., 1997: Boundary mixing and the dynamics of three-dimensional thermohaline circulations. *J. Phys. Oceanogr.,* **27,** 1713–1728.

Munk, W., 1966: Abyssal recipes. *Deep-Sea Res.,* **13,** 707–730.

——, and C. Wunsch, 1998: Abyssal recipes II: Energetics of tidal and wind mixing. *Deep-Sea Res.,* **45,** 1977–2010.

Osborn, T. R., 1980: Estimates of the local rate of vertical diffusion from dissipation measurements. *J. Phys. Oceanogr.,* **10,** 83–89.

Pinkel, R., and J. A. Smith, 1992: Repeat-sequence coding for improved precision of Doppler sonar and sodar. *J. Atmos. Oceanic Technol.,* **9,** 149–163.

Polzin, K. L., and E. Firing, 1997: Estimates of diapycnal mixing using LADCP and CTD data from I8S. *Int. WOCE Newsl.,* **29,** 39–42.

——, J. M. Toole, and R. W. Schmitt, 1995: Finescale parameterizations of turbulent dissipation. *J. Phys. Oceanogr.,* **25,** 306–328.

——, K. G. Speer, J. M. Toole, and R. W. Schmitt, 1996: Intense mixing of Antarctic Bottom Water in the equatorial Atlantic Ocean. *Nature,* **380,** 54–57.

——, J. M. Toole, J. R. Ledwell, and R. W. Schmitt, 1997: Spatial variability of turbulent mixing in the abyssal ocean. *Science,* **276,** 93–96.

——, E. Kunze, J. M. Toole, and R. W. Schmitt, 2002: The partition of finescale energy into internal waves and geostrophic motion. *J. Phys. Oceanogr.*, submitted.

Prater, M. D., 1991: A method for depth and temperature correction of expendable probes. *J. Atmos. Oceanic Technol.,* **8,** 888–894.

RDI, 1996: *Acoustic Doppler Current Profiler—Principles of Operation: A Practical Primer*. RD Instruments, 54 pp.

Roemmich, D., S. Hautala, and D. Rudnick, 1996: Northward abyssal transport through the Samoan Passage and adjacent regions. *J. Geophys. Res.,* **101,** 14 039–14 055.

Samelson, R. M., 1998: Large-scale circulation with locally enhanced vertical mixing. *J. Phys. Oceanogr.,* **28,** 712–726.

Sanford, T. B., R. G. Drever, J. H. Dunlap, and E. A. D'Asaro, 1982: Design, operation and performance of an expendable temperature and velocity profiler (XTVP). Applied Physics Lab Tech. Rep. 8110, University of Washington, 83 pp. [Available from Applied Physics Lab, University of Washington, 1013 NE 40th, Seattle, WA 98105–6698.]

——, E. A. D'Asaro, E. Kunze, J. H. Dunlap, R. G. Drever, M. A. Kennelly, M. A. Prater, and M. S. Horgan, 1993: An XCP user's guide and reference manual. Applied Physics Lab Tech. Rep. APL-UW TR 9309, University of Washington, 59 pp. [Available from Applied Physics Lab, University of Washington, 1013 NE 40th, Seattle, WA 98105–6698.]

Schott, F., J. Fischer, J. Reppin, and U. Send, 1993: On mean and seasonal currents and transports at the western boundary of the equatorial Atlantic. *J. Geophys. Res.,* **98,** 14 353–14 368.

Send, U., 1994: Accuracy of current profile measurements: Effect of tropical and midlatitude internal waves. *J. Geophys. Res.,* **99,** 16 229–16 236.

Smith, S. A., D. C. Fritts, and T. E. VanZandt, 1987: Evidence for a saturated spectrum of atmospheric gravity waves. *J. Atmos. Sci.,* **44,** 1404–1410.

Stramma, L., J. Fischer, and F. Schott, 1996: The flow field off southwest India at 8°N during the southwest monsoon of August 1993. *J. Mar. Res.,* **54,** 55–72.

Sun, H., and E. Kunze, 1999: Internal wave–wave interactions. Part II: Spectral energy transfer and turbulence production. *J. Phys. Oceanogr.,* **29,** 2905–2919.

Toole, J. M., K. L. Polzin, and R. W. Schmitt, 1994: Estimates of diapycnal mixing in the abyssal ocean. *Science,* **264,** 1120–1123.

Urick, R. J., 1967: *Principles of Underwater Sound for Engineers*. McGraw-Hill, 342 pp.

Wijesekera, H., L. Padman, T. Dillon, M. Levine, C. Paulson, and R. Pinkel, 1993: The application of internal-wave dissipation models to a region of strong forcing. *J. Phys. Oceanogr.,* **23,** 269–286.

Wilson, W. D., W. E. Johns, and M. D. Hendry, 1994: Measurements of current structure and transport in the Windward Islands Passages: 1991–1993. *Proc. Principal Investigators Meeting,* Princeton, NJ, Atlantic Climate Change Program, 168–172.